University of Verona & University of Grenoble Alpes

Master in Applied Mathematics

FEM resolution of a viscoelastic fluid model in an abrupt contraction

Applications to highly deformed biological living tissues

Candidate:
Sara Avesani

Thesis advisor:
Pierre Saramito

Research supervisors:
Prof. Ibrahim Cheddadi
PhD. student Nathan Shourick

Anno Accademico

Contents

1 Introduction **1**

2 Non singular log-conformation formulation for viscoelastic fluids **4**

2.1 Abstract 4

2.2 Mathematical formulation 4

2.3 Dimentionless problem and Boundary Conditions 7

3 Numerical results **11**

3.1 Abstract 11

3.2 Numerical validation 12

3.3 Exploration of the model 15

4 Comparison with biological data **23**

4.1 Abstract 23

4.2 Estimation of the Weissenberg number using the relaxation length 23

5 Conclusion **33**

A Slip boundary conditions **34**

Chapter 1

Introduction

Viscoelastic fluids exhibit both viscous (liquid-like) and elastic (solid-like) properties. The characteristic time, or relaxation time, plays a crucial role in determining the transition between solid-like and liquid-like behaviour: when the applied stress or deformation occurs over a short timescale compared to the relaxation time of the fluid, it behaves more like a solid, presenting predominantly elastic behaviour. It means that it deforms under stress but returns to its original shape once the stress is removed. Conversely, when the applied stress or deformation takes place over a timescale much longer than the relaxation time, the viscoelastic fluid behaves more like a liquid. In this regime, the material exhibits viscous behaviour, meaning it flows and deforms continuously under stress without fully recovering its original shape.

The challenge lies in describing the material's macroscopic behaviour, given that it is made up of long and flexible polymer molecules suspended in a solvent at a microscopic level. As a result, these materials fall into the category of non-Newtonian fluids, requiring modification of the constitutive equations from the Navier-Stokes problem.

Viscoelastic fluids gained significant importance in biology: the structure of biological tissues evolves in time due to processes like cell deformations and rearrangements. These complex dynamics are regulated through an interplay between genetics and mechanics. Detailed experiments have been completed by Sham Tlili, François Graner and Hélène Delanoë-Ayari in their paper *A microfluidic platform to investigate the role of mechanical constraints on tissue reorganization* [1], which is the biological reference for this thesis work. In their study, they conducted experiments involving the aspiration of embryonic cell aggregates through narrow sections in microfluidic channels (see Figure 1.1). This process induced substantial deformations in the cells, which were observed and analyzed using advanced microscopy techniques.

The motivation for this thesis work is to simulate and understand some of the experimental results presented in their study. The focus will primarily be on modeling the deformation of cells within the channel and analyzing the relaxation length of the viscoelastic material. The chosen approach involves the Oldroyd-B model [2], used to describe the macroscopic behaviour of a viscoelastic

fluid in an abrupt contraction (Figure 1.2).

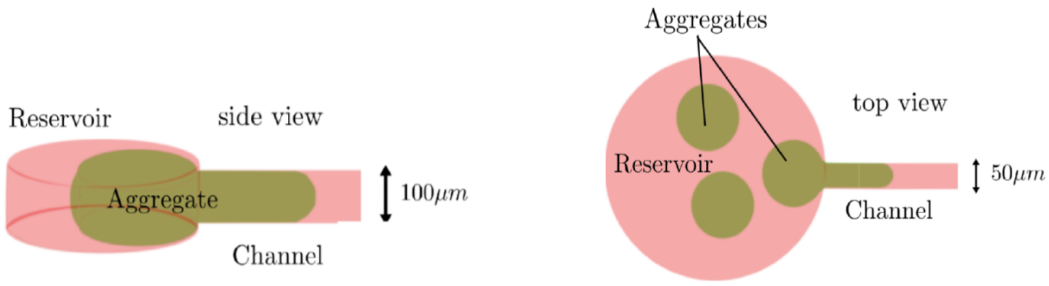

Figure 1.1: Geometry of the experiments.

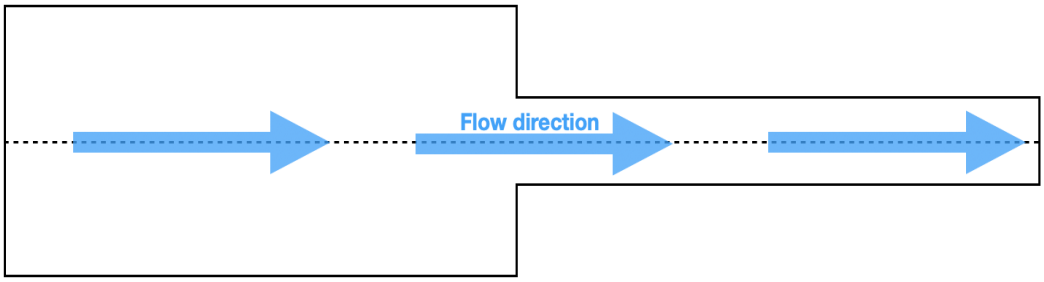

Figure 1.2: Geometry of the numerical resolution.

Chapter 2 introduces the viscolelastic fluid PDE formulation of the problem using the log-conformation formulation introduced by R. Fattal and R. Kupferman [3][4] and continued by Pierre Saramito in the paper *On a modified non-singular log-conformation formulation for Johnson–Segalman viscoelastic fluids* [5]. Given that the biological experiments involve the slip of the aggregate at the wall, my contribution for this chapter was to study the transition from stick to slip boundary conditions. The change of the wall boundary conditions from no-slip to slip significantly impacts the dynamics of the viscoelastic fluid, such as the evolution of the vortices at the corner, as will be explained in Chapter 3.

In details, Chapter 3 is dedicated to the numerical method, based on the C++ library *rheolef* [6]. An essential parameter in the studies of viscoelastic fluids is the Weissenberg number We, a dimensionless parameter that represents how much the elastic effects are preponderant compared to the viscous ones. The increase of Weissenberg number leads to stronger nonlinearities in the equations, which can make the simulation more challenging and computationally expensive to solve. However, using damped Newton method to directly achieve a stationary solution, led to some interesting results: the idea is to start from a small Weissenberg number and gradually increasing it by δWe to approach the desired higher parameter. In this chapter, I made some contributions: firstly, I validated the damped Newton model for the slip boundary condition, ensuring its accuracy. I also conducted a study on mesh convergence and compared vortices under

stick and slip boundary conditions. Additionally, I analyzed the deformation tensor by selectively cutting it along significant directions. In terms of the code, my main contribution was enabling the computation of solutions under slip boundary conditions. I also made some small upgrades to the data post-processing, enabling the extraction of both the conformation tensor and the elastic tensor, rather than only the elastic tensor.

Finally, in Chapter 4, the comparisons between the numerical results and the experimental data are made. An estimation of the most suitable Weissenberg number for the experiments is conducted by examining the velocity field and studying the conformation tensor.

Chapter 2

Non singular log-conformation formulation for viscoelastic fluids

2.1 Abstract

Viscoelastic fluids exhibit both viscous and elastic behaviour. At a microscopic level, polymer molecules are long and flexible chains that can be approximated using a spring model; on the other hand, describing the macroscopic behaviour of these polymer chains is one of the primary challenges in viscoelastic modelling.
Recall that an essential parameter in the studies of viscoelastic fluids is the Weissenberg number We that represents how much the elastic effects are preponderant compared to the viscous ones. The high Weissenberg number problem makes it difficult for numerical methods to accurately predict the behaviour of the fluid, especially at the walls and corners where singularities and gradient explosions occur. These phenomena lead to numerical errors, which become fatal when their accumulation affect the positive-definiteness of the conformation tensor, causing non physical solutions. In 2004, Fattal and Kupferman introduced the log-conformation formulation [3] [4], which represented a turning point for this problem. This formulation ensured positive-definiteness of the conformation tensor and linearization of the exponential stress profiles near singularities.
In this chapter, Pierre Saramito's formulation introduced in 2014 is considered. Although it involves a soft difference compared to Fattal and Kupferman's formulation, such as multiplication by a constant, it represents a more coherent change of variable as it is well-defined for all parameters. Before model the problem, look at the parameters and the variables in Tables 2.1 and 2.2.

2.2 Mathematical formulation

To model the problem, we use a PDE system consisting of three equations - the constitutive equation, continuity equation, and momentum equation - along with boundary and initial conditions. Consider

Table 2.1: Parameters

Parameter	Description	Unit
μ	elastic modulus of the material	Pa
η_v	solvent viscosity	$Pa \cdot s$
η_p	solvent-polymers viscosity	$Pa \cdot s$
λ	polymers relaxation time	s
a	parameter of the interpolated derivative	dimentionless

Table 2.2: Variables

Variable	Description	Unit
$\mathbf{u}$	velocity	$\frac{m}{s}$
p	pressure	Pa
$\boldsymbol{\tau}$	elastic tensor	Pa
$\mathbf{c} = \boldsymbol{\tau} + \frac{\eta_p}{a\lambda}\mathbf{I}$	conformation tensor	$\frac{N}{m^2}$
$\chi = \frac{\eta_p}{a\lambda}\log(\frac{a\lambda}{\eta_p}\mathbf{c})$	log-conformation tensor	$\frac{N}{m^2}$

the Maxwell satisfied by the elastic tensor $\boldsymbol{\tau}$:

$$\frac{1}{\mu}\frac{\mathcal{D}_a\boldsymbol{\tau}}{\mathcal{D}t} + \frac{\boldsymbol{\tau}}{\eta_p} = 2D(\mathbf{u}). \tag{2.1}$$

We study the Johnson-Segalman model, a variant of Oldroyd-B model, with mixed Gordon-Schowalter derivative:

$$\frac{\mathcal{D}_a\boldsymbol{\tau}}{\mathcal{D}t} = \frac{\partial\boldsymbol{\tau}}{\partial t} + (\mathbf{u}\cdot\nabla)\boldsymbol{\tau} - \boldsymbol{\tau}g_a(\mathbf{u})^T - g_a(\mathbf{u})\boldsymbol{\tau}, \tag{2.2}$$

where

$$g_a(u) = \frac{1+a}{2}\nabla\mathbf{u} - \frac{1-a}{2}\nabla\mathbf{u}^T, \tag{2.3}$$

Equation 2.1 can be also written in terms of the relaxation time $\lambda = \frac{\eta_p}{\mu}$:

$$\lambda\frac{\mathcal{D}_a\boldsymbol{\tau}}{\mathcal{D}t} + \boldsymbol{\tau} = 2\eta_p D(\mathbf{u}). \tag{2.4}$$

Let now introduce the conformation tensor $\mathbf{c}$:

$$\mathbf{c} = \boldsymbol{\tau} + \frac{\eta_p}{a\lambda}\mathbf{I}, \tag{2.5}$$

where $a \neq 0$ and $\lambda \neq 0$. This tensor represents the state of the microstructure of the medium under consideration: if the microconstituents (polymers or cells) do not relax, i.e. $\lambda = 0$, or deform under the effect of flow, i.e. $a = 0$, then the microstructure remains unchanged and the conformation tensor is undefined. It is worth noting that c is symmetric and positive definite [7], it has the dimension of a stress and is related to the direction $\mathbf{q}$ of the polymer chains at the microscopic scale through:

$$\mathbf{c} = c_0 \int_{\boldsymbol{q}\in\mathbb{R}^3} \boldsymbol{q} \otimes \boldsymbol{q}\psi(t, \boldsymbol{x}; \boldsymbol{q})\mathrm{d}q \tag{2.6}$$

where where c_0 is a positive constant and $\psi(t, \boldsymbol{x}; \boldsymbol{q})$ is the probability that the chain extends in the direction q at time t and at location x. Thus, the eigendirection associated to the largest eigenvalue of $\mathbf{c}$ is the most probable direction of the chain.
Finally, for the log-conformation formulation, consider the following change of variables:

$$\boldsymbol{\chi} = \frac{\eta_p}{a\lambda}\log\left(\frac{a\lambda}{\eta_p}\mathbf{c}\right) = \frac{\eta_p}{a\lambda}\log\left(\mathbf{I} + \frac{a\lambda}{\eta_p}\boldsymbol{\tau}\right). \tag{2.7}$$

The log-conformation formulation of the Johnson–Segalman problem reads:

$$\begin{aligned} \operatorname{div}\mathbf{u} = 0 \text{ in }]0, t_f[\times\Omega \\ \lambda\frac{D_0\boldsymbol{\chi}}{Dt} + \boldsymbol{\chi} - f\left(\frac{a\lambda}{\eta_p}, -\boldsymbol{\chi}\right) + \eta_p\kappa\left(\frac{a\lambda}{\eta_p}\boldsymbol{\chi}, 2D(\mathbf{u})\right) - 2\eta_p D(\mathbf{u}) = 0 \text{ in }]0, t_f[\times\Omega \\ \rho\frac{D\mathbf{u}}{Dt} - \operatorname{div}\left(\boldsymbol{\chi} + f\left(\frac{a\lambda}{\eta_p}, \boldsymbol{\chi}\right) + 2\eta_\nu D(\mathbf{u}) - p\cdot\mathbf{I}\right) = 0 \text{ in }]0, t_f[\times\Omega \end{aligned} \tag{2.8}$$

where $\kappa(\boldsymbol{\beta}, \boldsymbol{\gamma})$ is defined for all $\boldsymbol{\beta}, \boldsymbol{\gamma}$ symmetric real matrices by

$$\begin{aligned} \kappa(\boldsymbol{\beta}, \boldsymbol{\gamma}) &= \mathbf{q}\tilde{\kappa}\mathbf{q}^T \\ \tilde{\kappa}_{i,j} &= \hat{\kappa}\left(\frac{\beta_i - \beta_j}{2}\right)\tilde{\gamma}_{i,j}, \quad 1 \leqslant i, j \leqslant d \end{aligned}$$

where $\tilde{\boldsymbol{\beta}} = \mathbf{q}^T\boldsymbol{\beta}\mathbf{q} = \operatorname{diag}(\beta_i)$ and $\tilde{\gamma} = \mathbf{q}^T\gamma\mathbf{q}$. Here, $\hat{\kappa}(x)$ is defined for all $x \in \mathbb{R}$ by

$$\hat{\kappa}(x) = \begin{cases} 0 & \text{when } x = 0, \\ 1 - \frac{x}{\tanh(x)} & \text{otherwise.} \end{cases}$$

Moreover, for all real $\mu \geqslant 0$ and $\boldsymbol{\chi}$ symmetric real matrix

$$f(\mu, \boldsymbol{\chi}) = \begin{cases} 0 & \text{when } \mu = 0, \\ \frac{\exp(\mu\boldsymbol{\chi}) - \mathbf{I}}{\mu} - \boldsymbol{\chi} & \text{otherwise.} \end{cases}$$

Computing the logarithm of a tensor involves linear algebra methods like the diagonalization, the

study of the eigenvalues and eigenvectors. All the details to reach formulation 2.8 can be found in [5].

The initial conditions are:

$$\lambda\boldsymbol{\chi}(0) = \lambda\boldsymbol{\chi}_0 \text{ and } \mathbf{u}(0) = \mathbf{u}_0 \text{ in } \Omega \tag{2.9}$$

with $\boldsymbol{\chi}_0$ and $\mathbf{u}_0$ changing considering stick or slip setting.
While the benchmark problem may have prescribed stick boundary conditions, slip boundary conditions are better suited for the goals described in Chapter 3. Therefore, the formulation of the problem by Pierre Saramito [5] is now modified from stick to slip boundary conditions.

2.3 Dimentionless problem and Boundary Conditions

The geometry of the problem is known as an abrupt contraction, characterized by a large channel that narrows down into a smaller one at a single point. This geometry exhibits axis symmetry, making it convenient to solve the problem in only half of the domain, as in Figure A.1.

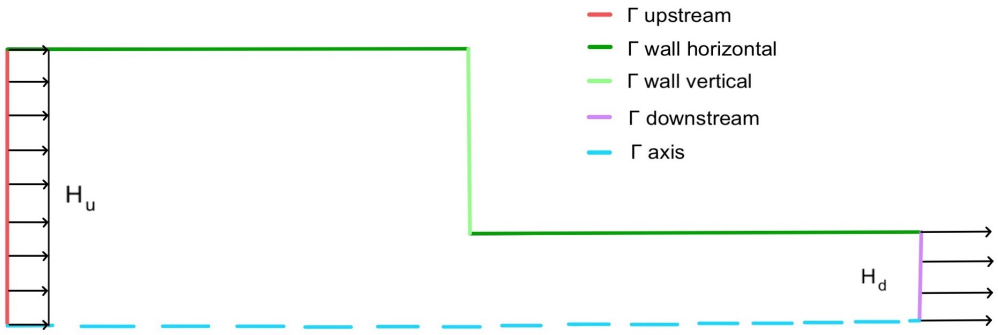

Figure 2.1: Geometry of the problem

Before exploring the slip boundary condition, it is convenient to adimentionalize problem 2.8 since the numerical parts uses the dimentionless varibales.
It is useful to come back to the classical formulation using the elastic tensor $\boldsymbol{\tau}$ to do this process, and then apply the changes of variable 2.5 and 2.7 on the dimentionless variables.
The problem in terms of $\boldsymbol{\tau}$ reads:

$$\begin{aligned} \operatorname{div}\mathbf{u} &= 0 \quad \text{in }]0,t_f[\times\Omega \\ \rho\left(\frac{\partial\mathbf{u}}{\partial t} + (\mathbf{u}.\nabla)\mathbf{u}\right) - \operatorname{div}\left(\boldsymbol{\tau} + 2\eta_p D(\mathbf{u}) - p\boldsymbol{I}\right) &= 0 \quad \text{in }]0,t_f[\times\Omega \\ \lambda\frac{\mathcal{D}_a\boldsymbol{\tau}}{\mathcal{D}t} + \boldsymbol{\tau} - 2\eta_v D(\mathbf{u}) &= 0 \quad \text{in }]0,t_f[\times\Omega \end{aligned} \tag{2.10}$$

Let us indicate the dimentionless variable with a tilde:

$$\tilde{\mathbf{x}} = \frac{\mathbf{x}}{\mathrm{L}} \qquad \tilde{\mathbf{u}} = \frac{\mathbf{u}}{\mathrm{V}} \qquad \tilde{\boldsymbol{\tau}} = \frac{\boldsymbol{\tau}}{\Sigma} \qquad \tilde{p} = \frac{p}{\Sigma} \tag{2.11}$$

where $\mathrm{L} = \mathrm{H_d}$, $\mathrm{V} = \frac{2c}{3}\mathrm{U}_{u,max}$ and $\Sigma = (\eta_v + \eta_p)\frac{V}{L}$. For these computations see [8].
We have that the mass conservation equation in 2.10 becomes:

$$\mathrm{L}^{-1}\,\mathrm{div}\left(\frac{\mathbf{u}}{\mathrm{V}}\right) = 0$$

$$\tilde{\mathrm{div}}(\tilde{\mathbf{u}}) = 0 \tag{2.12}$$

Regarding the momentum equation in 2.10, let us take as convention $(\mathbf{u}.\nabla)\mathbf{u} = 0$ and, since we study the steady solution, $\frac{\partial \mathbf{u}}{\partial t} = 0$. Dividing the equation by ΣL and we obtain

$$\mathrm{L}^{-1}\,\mathrm{div}\left(\frac{\boldsymbol{\tau}}{\Sigma} + \frac{2\eta_p D(\mathbf{u})}{\Sigma} - \frac{p}{\Sigma}\boldsymbol{I}\right) = 0$$

$$\tilde{\mathrm{div}}\left(\tilde{\boldsymbol{\tau}} + 2\frac{\eta_p}{\eta_p + \eta_v}\tilde{D}(\tilde{\mathbf{u}}) - \tilde{p}\boldsymbol{I}\right) = 0$$

The parameter $\frac{\eta_v}{\eta_p+\eta_v}$ is called in literature α, thus we have:

$$\tilde{\mathrm{div}}\left(\tilde{\boldsymbol{\tau}} + 2(1-\alpha)\tilde{D}(\tilde{\mathbf{u}}) - \tilde{p}\boldsymbol{I}\right) = 0 \tag{2.13}$$

Finally, we can adimentionalize the constitutive equation in 2.10 dividing by Σ:

Hence, he dimentionless problem reads:

$$\begin{aligned} \tilde{\mathrm{div}}(\tilde{\mathbf{u}}) &= 0 \quad \text{in }]0, t_f[\times\Omega \\ \tilde{\mathrm{div}}\left(\tilde{\boldsymbol{\tau}} + 2(1-\alpha)\tilde{D}(\tilde{\mathbf{u}}) - \tilde{p}\boldsymbol{I}\right) &= 0 \quad \text{in }]0, t_f[\times\Omega \\ We\frac{\tilde{\mathcal{D}}_a\tilde{\boldsymbol{\tau}}}{\tilde{\mathcal{D}}\tilde{t}} + \tilde{\boldsymbol{\tau}} - 2\alpha\tilde{D}(\tilde{\mathbf{u}}) &= 0 \quad \text{in }]0, t_f[\times\Omega \end{aligned} \tag{2.14}$$

To conclude, we apply the change of variable to obtain $\tilde{\mathbf{c}}$ and $\tilde{\boldsymbol{\chi}}$:

$$\tilde{\mathbf{c}} = \frac{\mathbf{c}}{\Sigma} = \tilde{\boldsymbol{\tau}} + \frac{\eta_v}{\lambda\,(\eta_v + \eta_p)\,\frac{\mathrm{V}}{\mathrm{L}}}I = \tilde{\boldsymbol{\tau}} + \frac{\alpha}{We}I \tag{2.15}$$

2.3. Dimentionless problem and Boundary Conditions

$$\begin{aligned}\tilde{\boldsymbol{\chi}} = \frac{\boldsymbol{\chi}}{\Sigma} &= \frac{\eta_v}{\lambda\left(\eta_v+\eta_p\right)\frac{\mathrm{V}}{\mathrm{L}}}\log\left(\frac{a\lambda}{\eta_v}\,\tilde{\mathbf{c}}\,\Sigma\right) \\ &= \frac{\alpha}{We}\log\left(\frac{We}{\alpha}\tilde{c}\right)\end{aligned} \tag{2.16}$$

Regarding the boundary conditions, they have been developed in [5], and the computations for the slip case can be found in Appendix A.

To sum up all the computations in appendix, see Figure 2.2. For the stick case, let us define what are $\mathbf{u}_{\mathrm{u}}$, $\mathbf{u}_{\mathrm{d}}$ and τ_{u}. We require that the velocity upstream and downstream follow the Poseuille profile; thus, considering the dimentionless components, we have that, for the abrupt contraction:

$$\mathbf{u}_{\mathrm{u}} = \frac{3}{2c}\left(1-\left(\frac{y}{c}\right)^2\right) \tag{2.17}$$

$$\mathbf{u}_{\mathrm{d}} = \frac{3}{2}\left(1-y^2\right) \tag{2.18}$$

$$\tau_{xx} = \frac{18\,\alpha\,We\,y^2}{c^6} \tag{2.19}$$

$$\tau_{xy} = -\frac{3\,\alpha\,y}{c^3} \tag{2.20}$$

$$\tau_{yy} = 0 \tag{2.21}$$

Equations (2.17) and (2.18) come from the Poiseuille solution in a 2d pipe (see [9], section 1.5) while equations (2.19)-(2.21) are specific to the Poiseuille flow in an abrupt contraction (see [9], section 4.4).

To better illustrate the contrast between them, we can create a heatmap that represents the magnitude of the velocity field, in Figure 2.3. By examining this visualization, we can observe distinct patterns: for the stick condition, the velocity is zero at the wall, while for the slip condition, the velocity reaches a constant value of 1 downstream and of $\frac{1}{c} = \frac{\mathrm{H_d}}{\mathrm{H_u}}$ upstream. In our specific geometry, $\frac{\mathrm{H_d}}{\mathrm{H_u}}$ is equal to $\frac{1}{4}$.

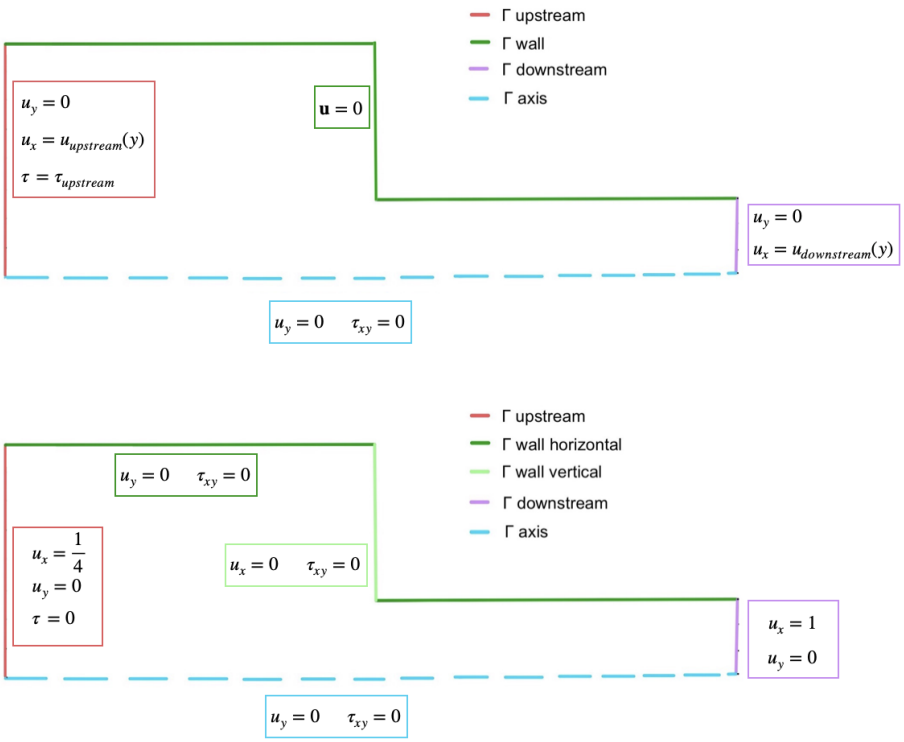

Figure 2.2: Stick and slip boundary conditions summary.

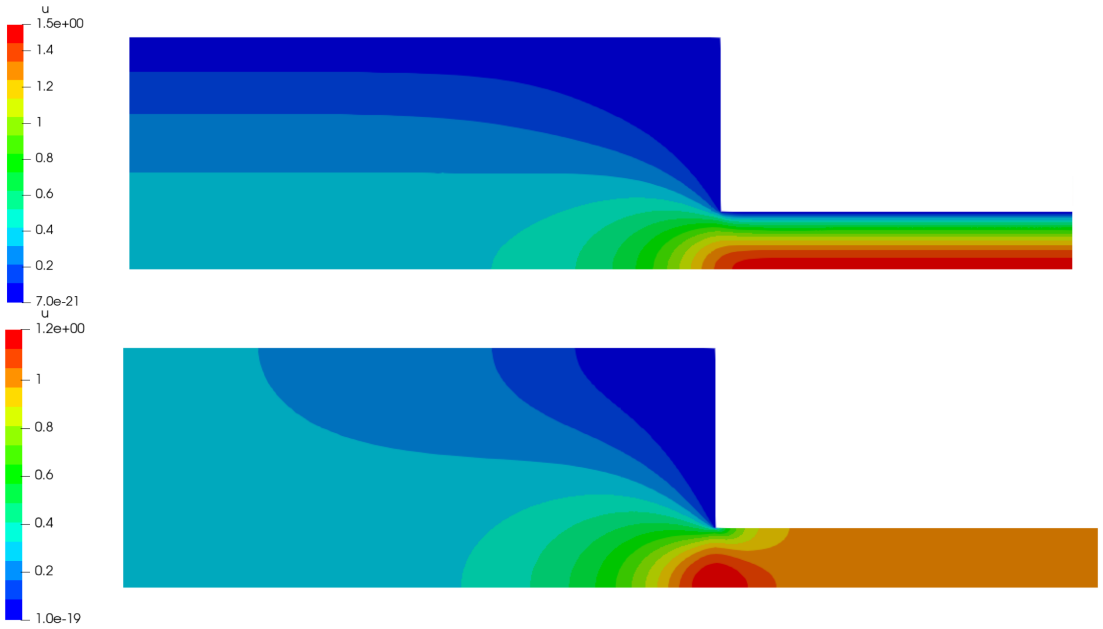

Figure 2.3: Velocity heat map with $We = 0.3$. Above: stick boundary conditions, below: slip boundary conditions.

Chapter 3

Numerical results

3.1 Abstract

In this chapter, the numerical scheme is described, followed by the numerical validation, which involves studying the mesh convergence and comparing the numerical solution with the exact solution downstream. Lastly, the model is explored with varying the Weissenberg number, where the study focuses on vortices, maximum deformation, and relaxation length in the small channel. In our experimental setup, both the large and small channels have a length of 20 units. Regarding the height, the large channel has a height of 4 units, while the height of the small channel remains fixed at 1 unit. Moreover, the parameter a of the derivative is set at 1 since we take into account the Oldroyd-B model and the parameter α is fixed to $\frac{8}{9}$.

Only a few authors in the literature have made significant progresses in understanding this problem. Specifically, for Weissenberg numbers (We) ranging from 6 to 14, there is no established theory regarding the behavior of the fluid. To be more precise, for We values between 0 and 6, a stable and symmetrical solution exists; on the other hand, for We values greater than 14, an oscillating and asymmetric behavior occurs. This results in the formation of small and large vortices in the upper and lower corners of the fluid, which interchange over time [10]. However, in considering Comminal's paper, they studied the time-dependent problem with greater regularity by reformulating it using the stream function.

In this thesis, the code is built using the Rheolef library, which performs a damped Newton algorithm to compute the stationary solution. See the Rheolef user's guide [6], section 3.2.4, for a complete presentation of the damped Newton method. The aim is to obtain a globally convergent algorithm by decreasing the step length and, at the same time, maintaining the direction of the classical Newton algorithm.

Consider the unknown $\mathbf{X} = [\boldsymbol{\chi} \quad \mathbf{u} \quad p]^T$ and F given by the left hand side of equation 2.14 after having applied the change of variable with $\boldsymbol{\chi}$. Instead of directly updating the estimate with the classical Newton method, the algorithm scales down the update by multiplying it with a damping

factor λ_n less than 1:

$$\mathbf{X}^{n+1} = \mathbf{X}^n + \lambda_n \delta \mathbf{X}^n$$

where $\delta \mathbf{X}^{(n)}$ is the direction of Newton algorithm, given by:

$$F'(\mathbf{X}^n)\delta \mathbf{X}^n = -F(\mathbf{X}^n)$$

The algorithm stops when the residual is less that a fixed tolerance.

3.2 Numerical validation

Three different mesh refinements were used for the simulations, and their properties are presented in Table 3.1, while their visual representations are shown in Figure 3.1. A P2 polynomial approximation is used for the velocity, while a P1 discontinuous polynomial approximation is used for both the elastic tensor τ and the pressure. This velocity-pressure pair do not satisfy the inf-sup condition and the Arnold and Qin macro element method is used to overcome this problem [5]: each triangle in the mesh is subdivided into three different sub-triangles using the barycenters.

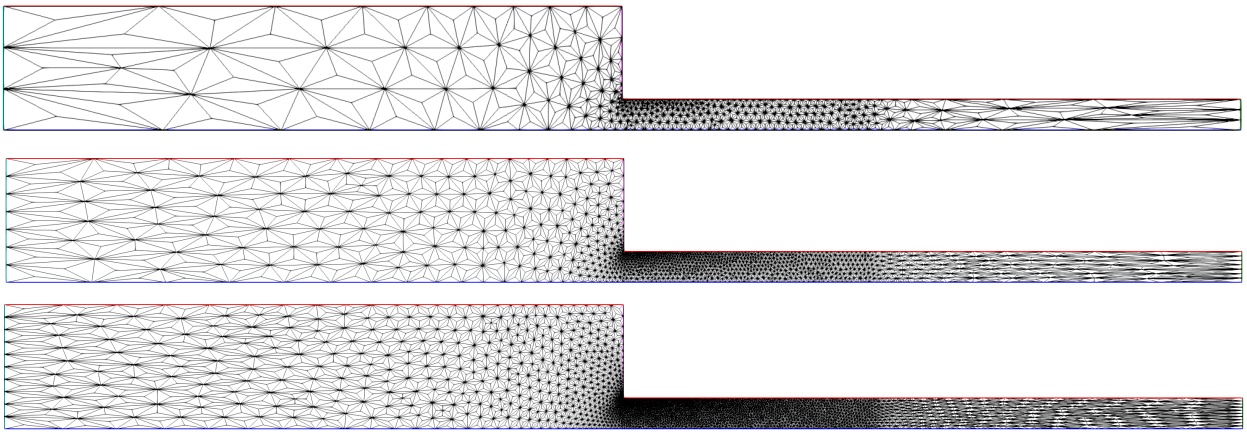

Figure 3.1: Mesh1 (above), Mesh2 (center) and Mesh3 (below), see Table 3.1 for details.

Table 3.1: Mesh properties

	Mesh1	**Mesh2**	**Mesh3**
Minimum triangle size	0.053	0.022	0.014
Maximum triangle size	6.676	3.250	2.363
Number of vertices	759	2890	6726
Number of elements	1398	5541	13095

3.2. Numerical validation

One initial step in numerical analysis is to assess mesh convergence. This involves examining how the solution behaves when the Weissenberg number remains constant while the mesh resolution is adjusted. Initially, we can evaluate mesh convergence by observing the velocity and the elastic tensor. The idea is to cut them along the axis of symmetry and determine whether the behaviour becomes more stable (with fewer oscillations) as the mesh is refined. Figures 3.2 and 3.3 illustrate this behaviour, demonstrating that a denser mesh leads to a more stable solution, with less oscillations.

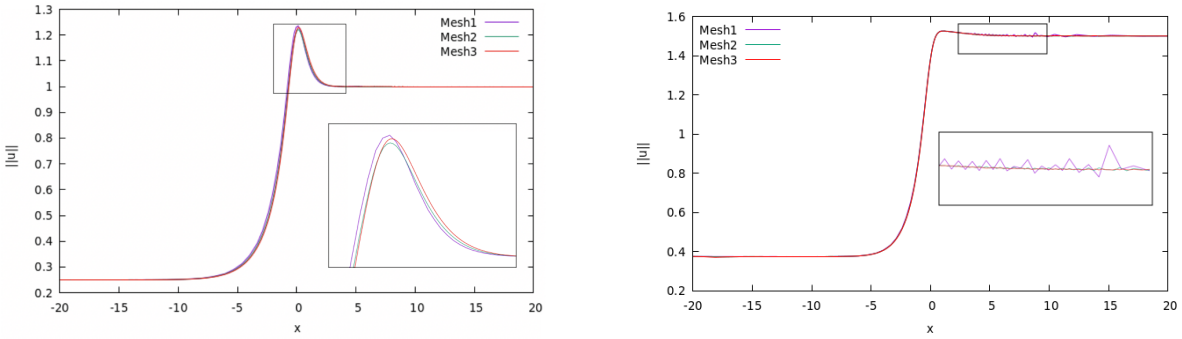

Figure 3.2: Velocity along horizontal axis with Mesh refinement, fix $We = 1$. Left: slip case, Right: stick case. In the black boxes: zoom on significant regions.

The second step consists into comparing the numerical velocity with the Poiseuille velocity closed to downstream, in order to check if the small channel is long enough. For the slip boundary condition, the velocity downstream remains constant at 1 in the horizontal direction, while for the stick boundary condition, a parabolic velocity profile is obtained downstream (see equation (2.18)). The idea is to observe the numerical velocity profiles at $x = 15$: if they are closed to the exact solutions, then we can conclude that the chosen channel length, i.e. 20, is sufficient. To visualize the velocity with respect to the channel, where the vertical axis represents the variable y and the horizontal axis represents the velocity $u(y)$, we can invert equation (2.18):

$$y = \sqrt{1 - \frac{2}{3}u(y)} \tag{3.1}$$

The results for different meshes and fixed $We = 2$ are in Figure 3.4. To assess the accuracy of the numerical solution compared to the exact solution, we examine the absolute difference between the two velocities, as shown in Figure 3.5. As the mesh becomes finer, the velocity profiles are more stable, so here is another confirmation of the mesh convergence.

In both cases of slip and stick boundary conditions, we observe an error that is less than 2%. In the slip case, a block transition of the fluid is observed at the position $x = 15$, while in the stick case, a parabolic fluid motion is observed with the velocity reaching its maximum at the axis of symmetry. These findings indicate that the channel length is sufficient.

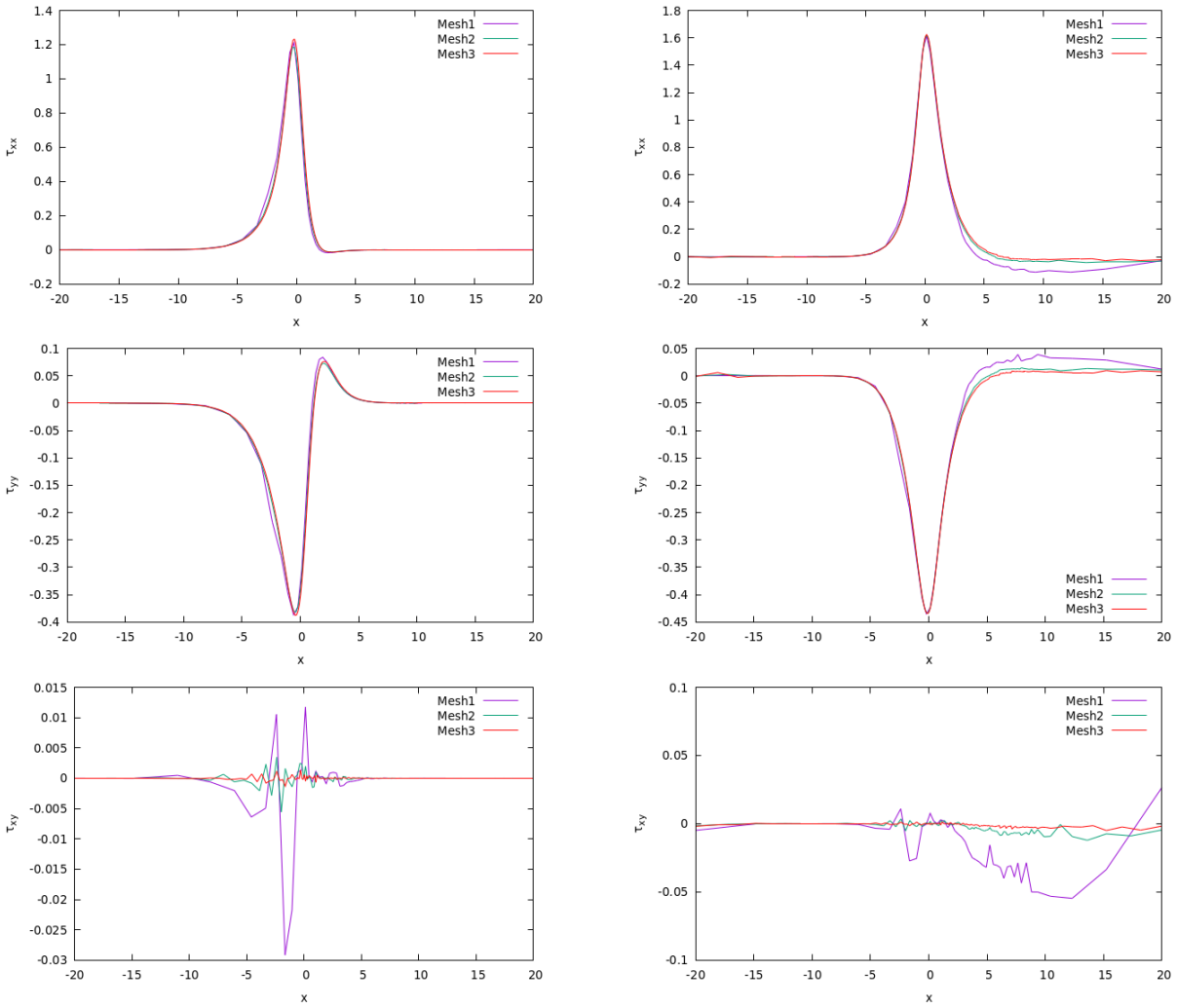

Figure 3.3: Elastic tensor along horizontal axis with Mesh refinement, fix $We = 1$. Left: slip case, Right: stick case. From above to below: τ_{xx}, τ_{yy} and τ_{xy}.

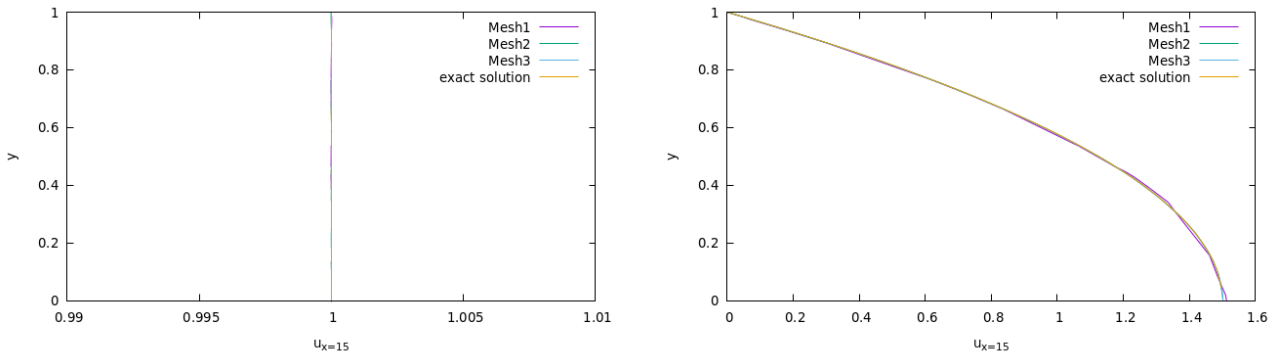

Figure 3.4: Velocity downstream for different Meshes fixed $We = 2$. Left: slip case, Right: stick case.

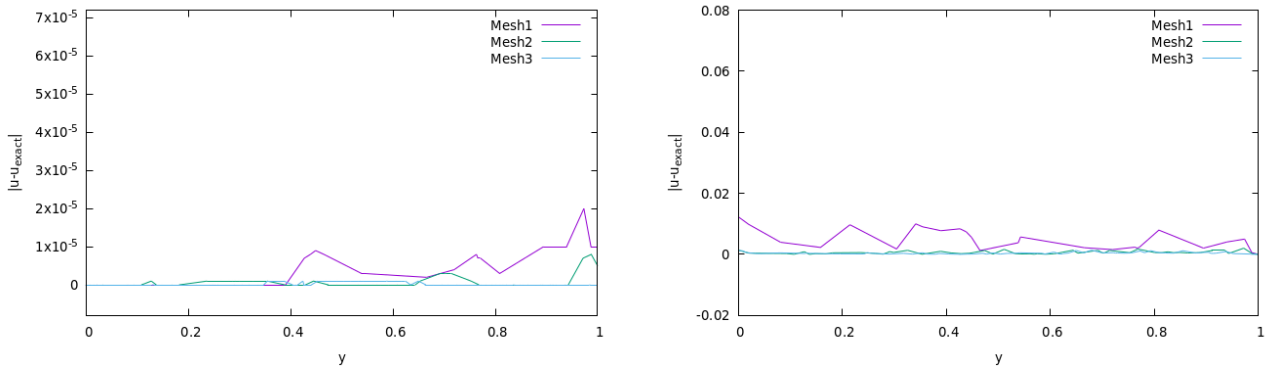

Figure 3.5: $|u_{\text{numerical}} - u_{\text{exact}}|$. Left: slip case, Right: stick case.

3.3 Exploration of the model

In this section, our focus lies on visualizing the vortices by studying the streamlines under slip and stick boundary conditions. This allows us to observe practical differences between these two types of boundary conditions. Moreover, we start to investigate the properties of the deformation tensor. After solving the variational formulation problem (2.8) in terms of $\boldsymbol{\chi}$, it is straightforward to obtain $\boldsymbol{\tau}$ using the inverse formula of (2.7):

$$\boldsymbol{\tau} = \frac{\eta_p}{a\lambda}\left(\exp\left(\frac{a\lambda}{\eta_p}\boldsymbol{\chi}\right) - I\right) \tag{3.2}$$

In particular, using the elastic tensor, it is interesting to analyze the deformation $\boldsymbol{\epsilon}^e = We \cdot \boldsymbol{\tau}$. Starting from the stream function, recall its definition:

Definition 3.3.1 (Stream function)
Let $\mathbf{u}$ *be the divergence free velocity field associated to problem* (2.8). *The stream function* ϕ *is a scalar field that satisfies*

$$\nabla\phi = curl(\mathbf{u}) \quad in\ \Omega$$

$$\phi = 0 \quad in\ \partial\Omega$$

This function proves to be highly beneficial in detecting vortices, particularly in the upper and entrance corners. Figures 3.6 and 3.7 show the streamlines under slip and stick boundary conditions. In the slip case, we observe a larger vortex forming in the upper corner. The maximum We reached in the numerics is around 10 with Mesh3 in this case. On the other hand, under stick conditions, two initial vortices arise (noticeable for $We \sim 3$) and, subsequently, they merge together. The maximum We number is 2.7 with the finer Mesh3, 3 with Mesh2 and 6 with Mesh1.

Another useful aspect to take into account for the experiments in the following chapter is the maximum elongation of the polymers: this can be detected by observing the behaviour of the

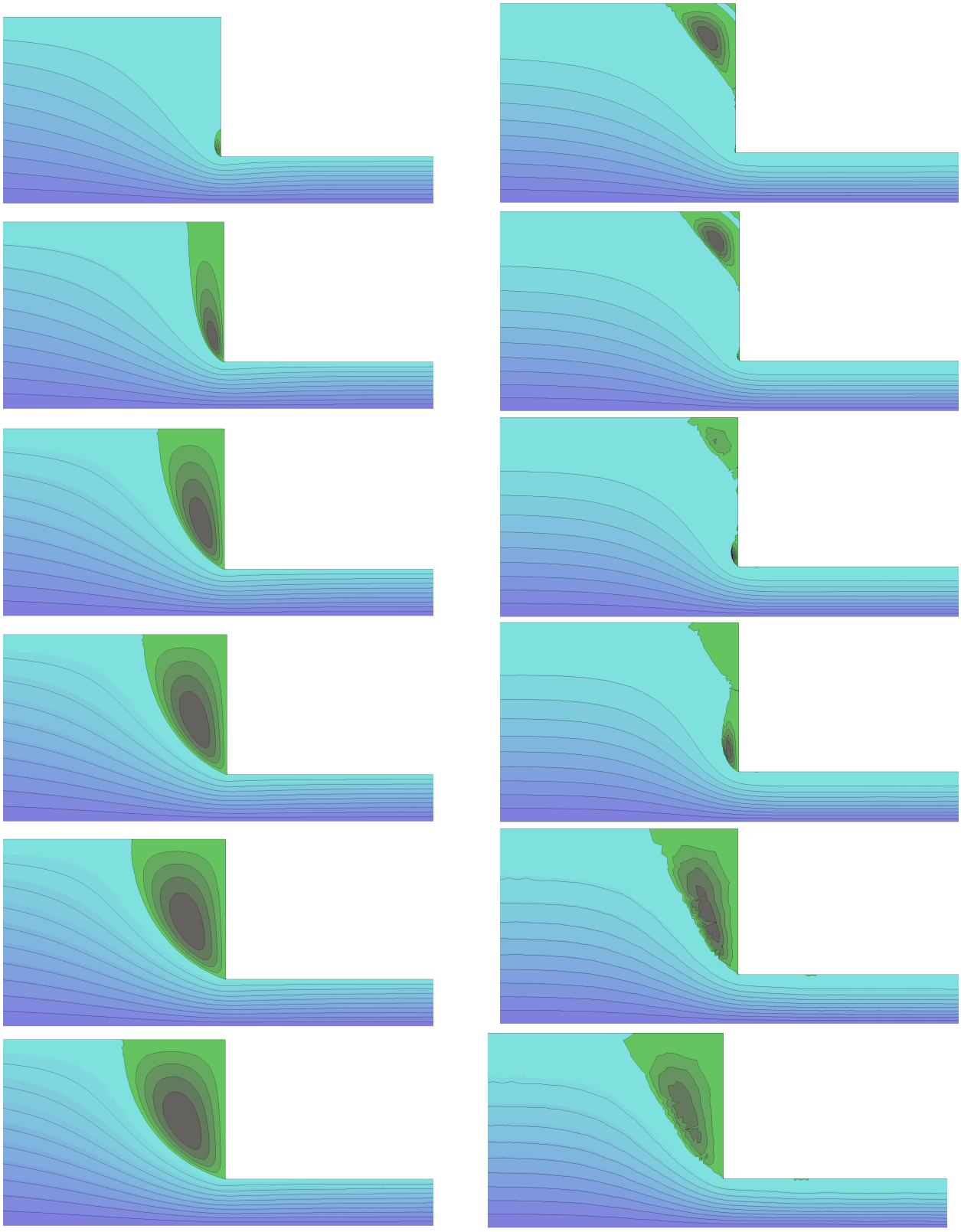

Figure 3.6: Isolines of the stream function for slip (left) and stick (right) boundary conditions. From above to below, $We = 1, 2, 3, 4, 5, 6$. For the slip case, only the Mesh3 is used, while for the stick case, since for Mesh3 the maximum Weissenberg number reachable is around 3, the case with $We = 4, 5, 6$ use Mesh1.

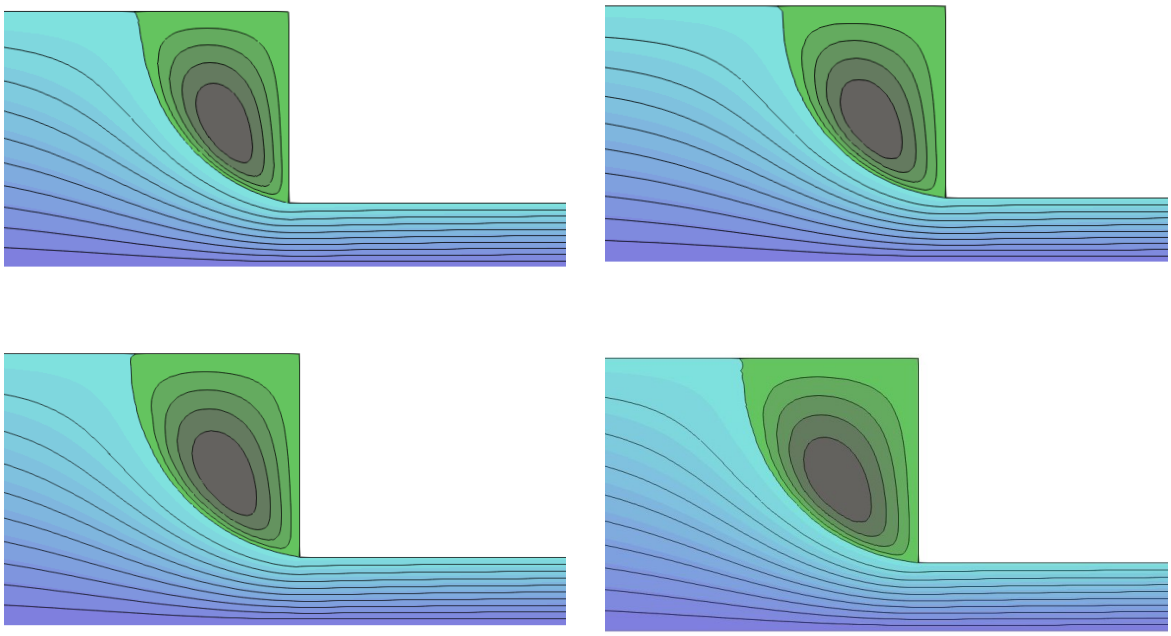

Figure 3.7: Isolines of the stream function for slip boundary conditions with $We = 7, 8, 9, 10$, from top left to bottom right.

deformation tensor in some significant directions along the channels. Recall that the difference between the xx and yy component of the deformation tensor represents the isotropic deformation. In details, when it is positive, an higher elongation in the x direction is expected, while a negative values represents a more pronounced elongation in the y direction. On the other side, the sum of the diagonal components represent the compression of the cells or polymers.

We explore two interesting directions in our analysis. First, we examine the horizontal direction along the axis of symmetry, as shown in Figure 3.8. The corresponding deformation tensor for both slip and stick conditions is displayed in Figure 3.9. As expected, the magnitude of the deformation tensor increases with the Weissenberg number, indicating a more elastic behaviour. Additionally, in the stick case, we observe higher deformation values due to the adhesion of certain cells to the wall.

Next, we focus on the vertical direction near the entrance, as depicted in Figure 3.10. The corresponding results can be seen in Figure 3.11.

To quantify the maximum deformation along the horizontal direction, refer to Figure 3.12. Similarly, Figure 3.13 provides the maximum deformation along the vertical axis. It is worth noting that in some plots, the minimum deformation is also depicted if it is significant. In cases where it is not represented, the minimum deformation is close to zero for each Weissenberg number and therefore considered irrelevant.

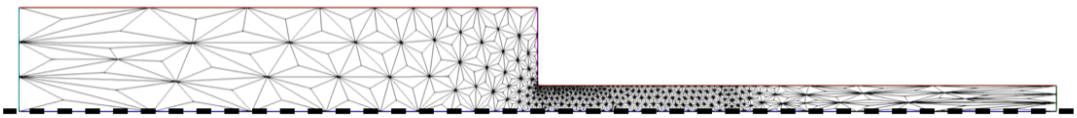

Figure 3.8: First significant direction where to observe the behaviour of the deformation tensor: axis of symmetry of the domain.

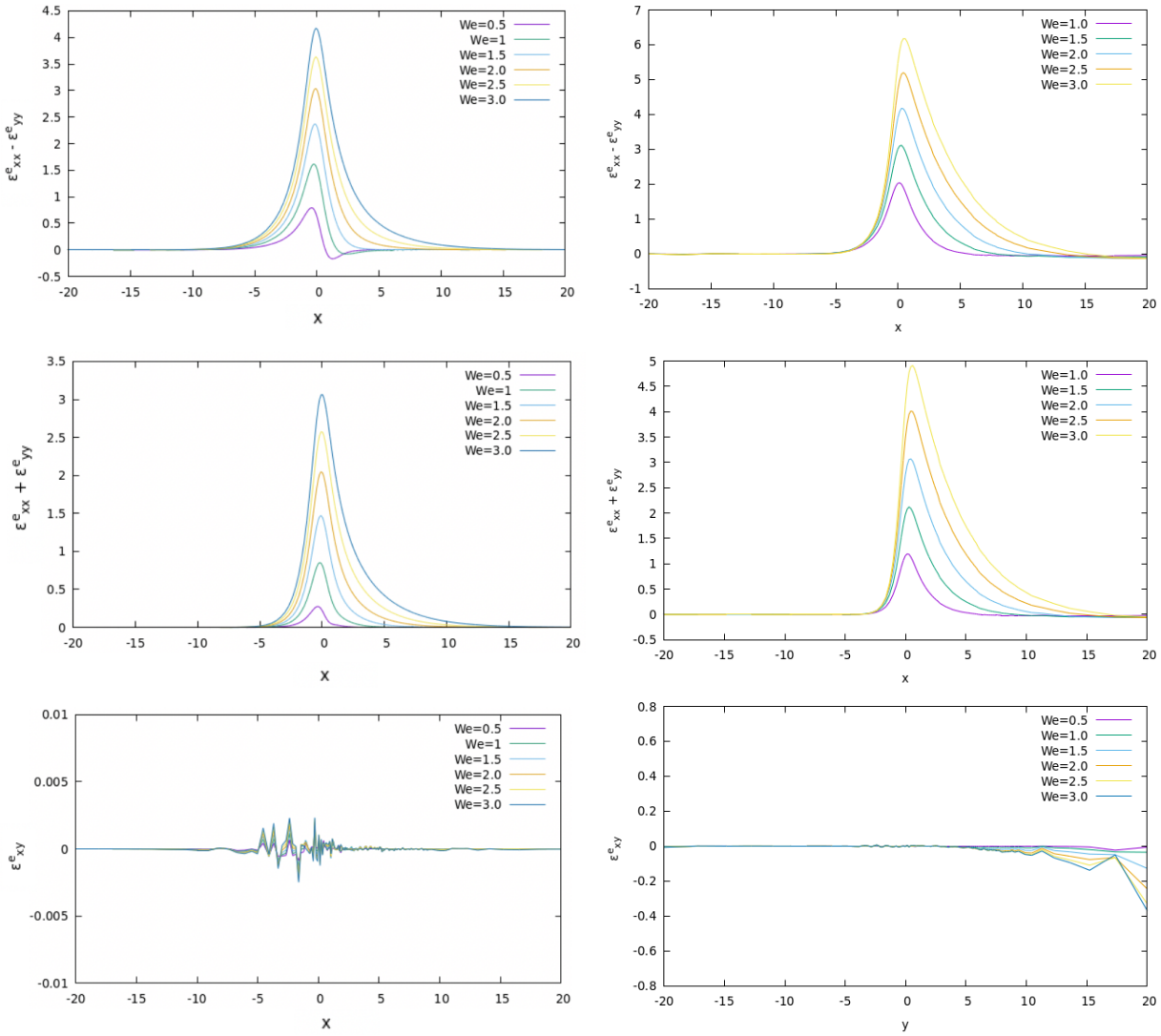

Figure 3.9: Cut of the deformation along the horizontal axis of symmetry. From above to below: $\epsilon^e_{xx} - \epsilon^e_{yy}$, $\epsilon^e_{xx} + \epsilon^e_{yy}$ and the shear deformation ϵ^e_{xy}. Left: slip case, right: stick case. Used meshes: Mesh3 for slip case, Mesh2 for stick case.

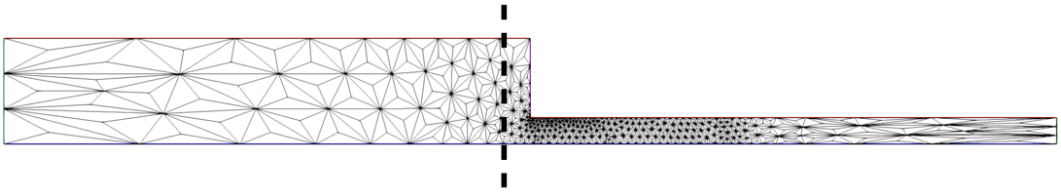

Figure 3.10: Second significant direction where to observe the behaviour of the deformation tensor: vertical direction in the vicinity of the corner. Note that this direction is preferable to the one passing through the singularity in order to avoid the explosion of the deformation.

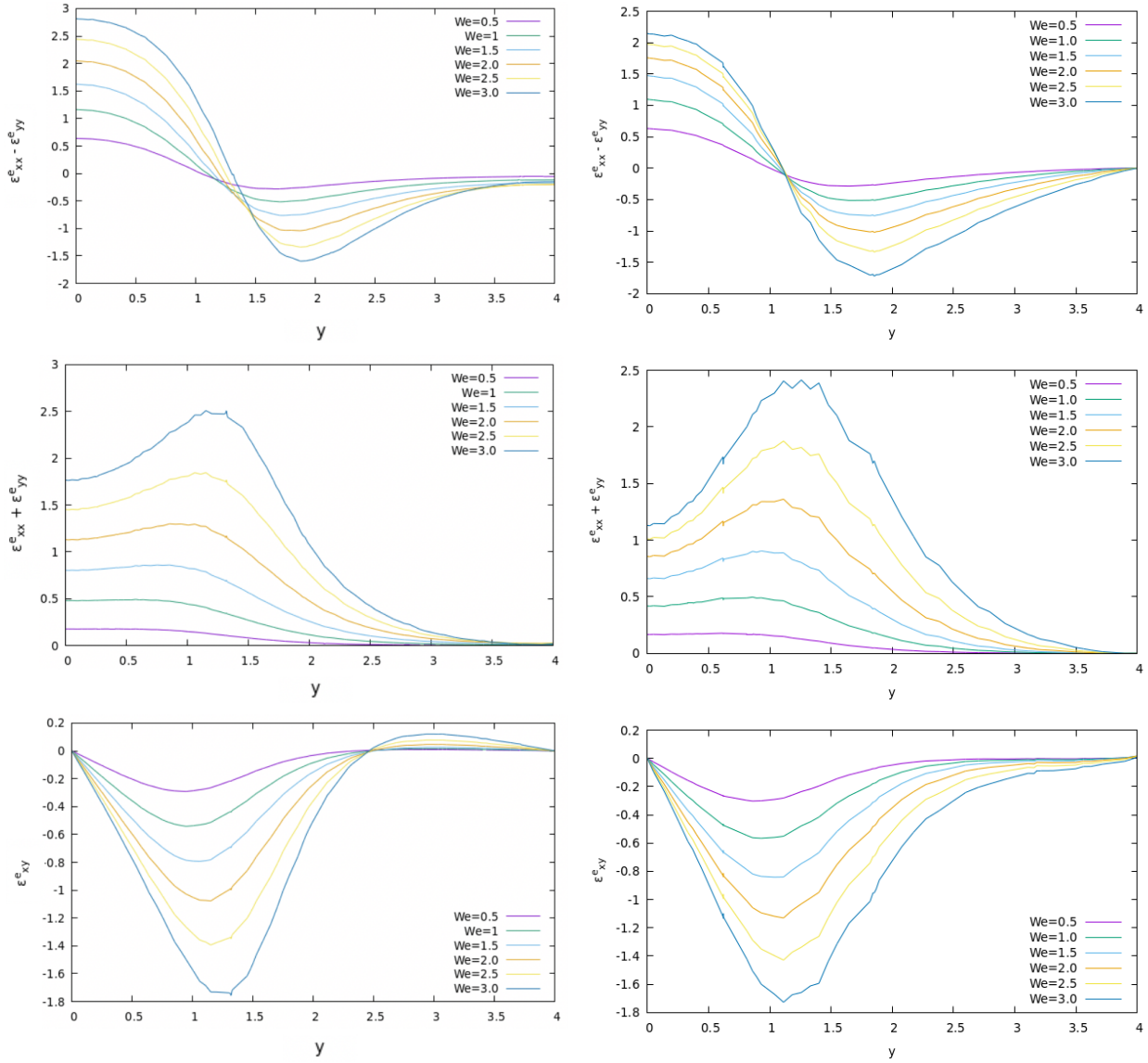

Figure 3.11: Cut of the deformation along the vertical axis near the corner. From above to below: $\epsilon^e_{xx} - \epsilon^e_{yy}$, $\epsilon^e_{xx} + \epsilon^e_{yy}$ and the shear deformation ϵ^e_{xy}. Left: slip case, right: stick case. Used meshes: Mesh3 for slip case, Mesh2 for stick case.

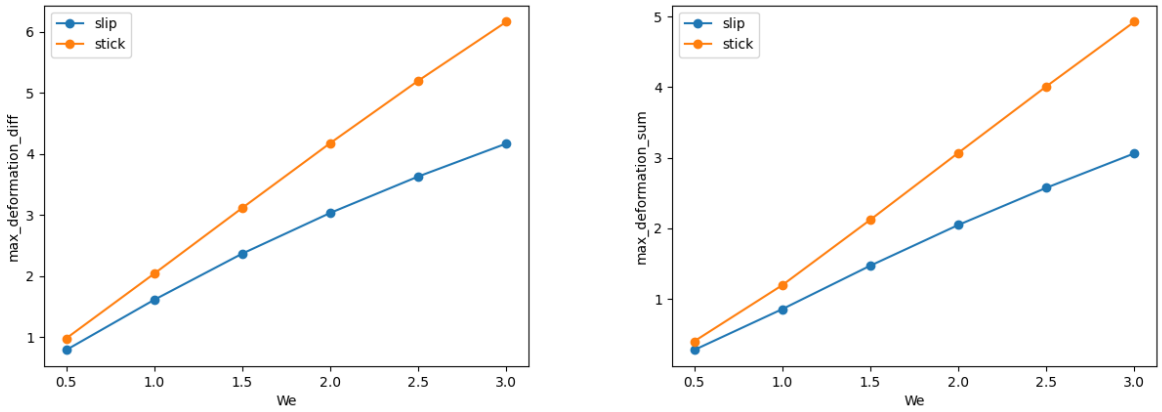

Figure 3.12: Maximum value of $\epsilon^e_{xx} - \epsilon^e_{yy}$ (right) and $\epsilon^e_{xx} + \epsilon^e_{yy}$ (left) along the horizontal direction. The shear deformation ϵ^e_{xy} is not plotted since it is really closed to 0 for each We number.

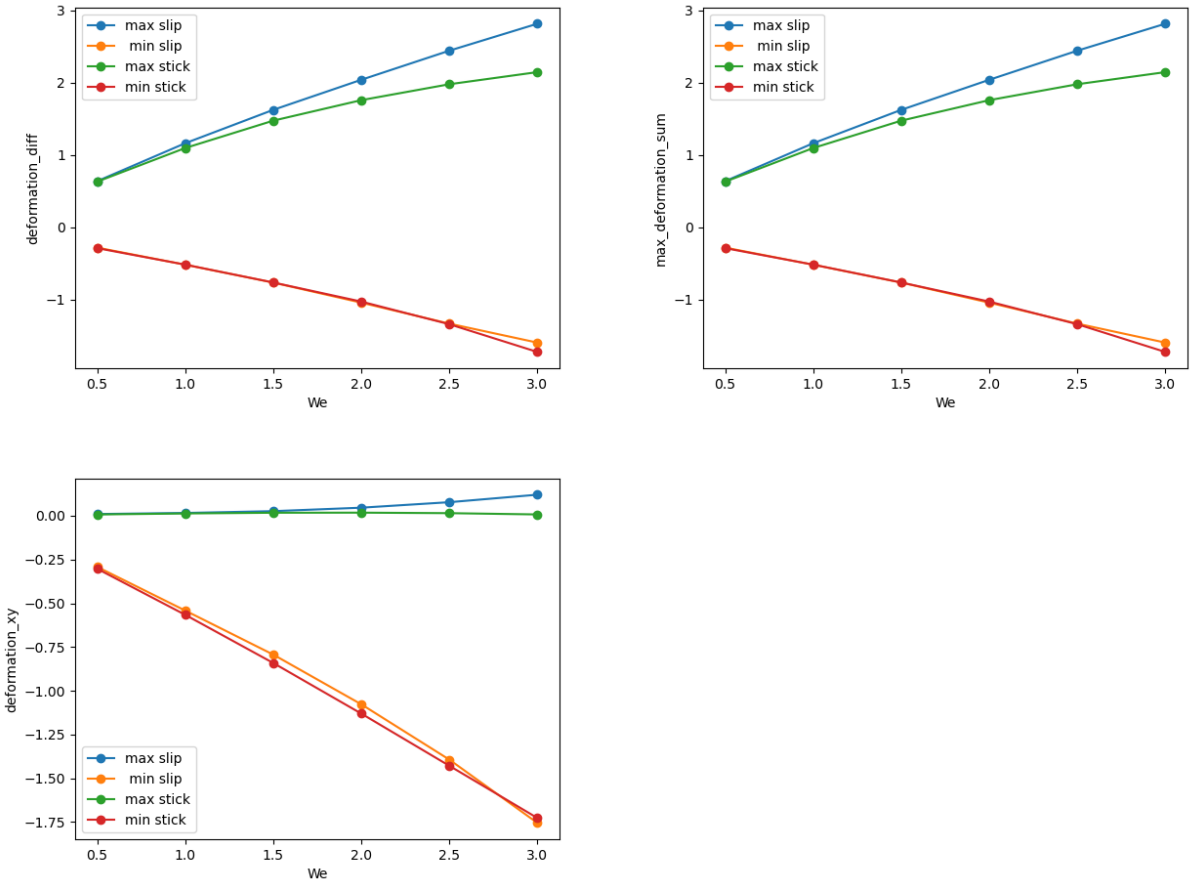

Figure 3.13: Above left: maximum value of $\epsilon^e_{xx} - \epsilon^e_{yy}$, above right: maximum value of $\epsilon^e_{xx} + \epsilon^e_{yy}$, below: maximum value of ϵ^e_{xy} along the vertical direction.

The last crucial aspect is understanding the behaviour near the singularity, particularly at the entrance corner. The model states that the velocity gradient explodes near the singularity, implying a substantial increase in the deformation tensor. Specifically, Figure 3.15 illustrates the maximum value of the tensor in both the slip and stick cases, made by cutting the deformation tensor along the horizontal axis passing through the singularity and taking the peak value. It is worth noting that in the slip case, the growth appears to be linear, whereas in the stick case, it becomes exponential after a Weissenberg number of approximately 5. A possible explanation for this phenomenon is that in the stick case, with the fluid adhering to the wall and having significant elasticity, the cells stretch while being fixed at the corner, leading the deformation tend fast to infinity. On the other hand, in the slip case, although the deformation still increases, the slip factor at the wall helps contain the exponential explosion.

Figure **??** illustrates the logarithm of the absolute value of the deformation tensor specifically for the slip case. We focus on the slip boundary conditions because it appears that the deformation does not exhibit an exponential decrease along the axis under consideration in the stick case. In the plot of the logarithm of the absolute value of the deformation tensor, the slope of the curves can provide insights into the rate of change of the deformation. Specifically, a steeper slope indicates a more rapid decrease or increase in the deformation, implying a higher rate of deformation change. On the other hand, a gentler slope suggests a slower change in the deformation magnitude along the axis. For higher We numbers, the slope is expected to be lower, because the cells take more time to return to their original shape, i.e. the relaxation time is slower, so the deformation is less rapid. To observe in deeper details this behaviour, Figure 3.16 plot the deformation tensor for $We = 1, 2, 3$. Even if the representations are not so clean, they are useful to understand what the explosion of the velocity gradient causes: the deformation in the corner tends to infinity as We increases.

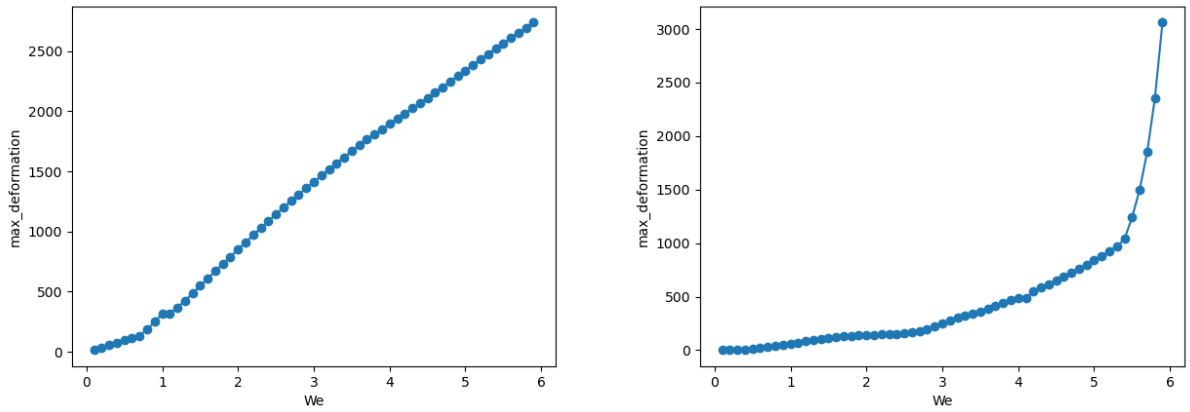

Figure 3.14: Maximum deformation at the corner vs We. Left: slip case, Right: stick case.

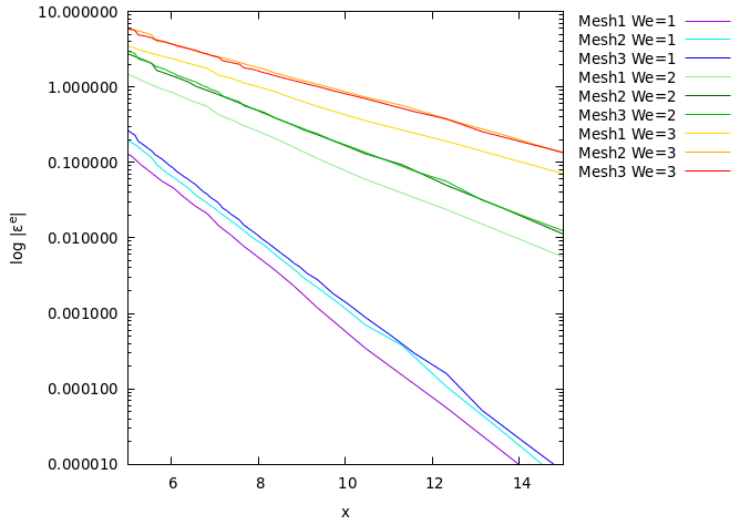

Figure 3.15: Plot of logarithm of absolute value of the deformation tensor for different Meshes and different We numbers. The x axis is cut in $[5, 15]$.

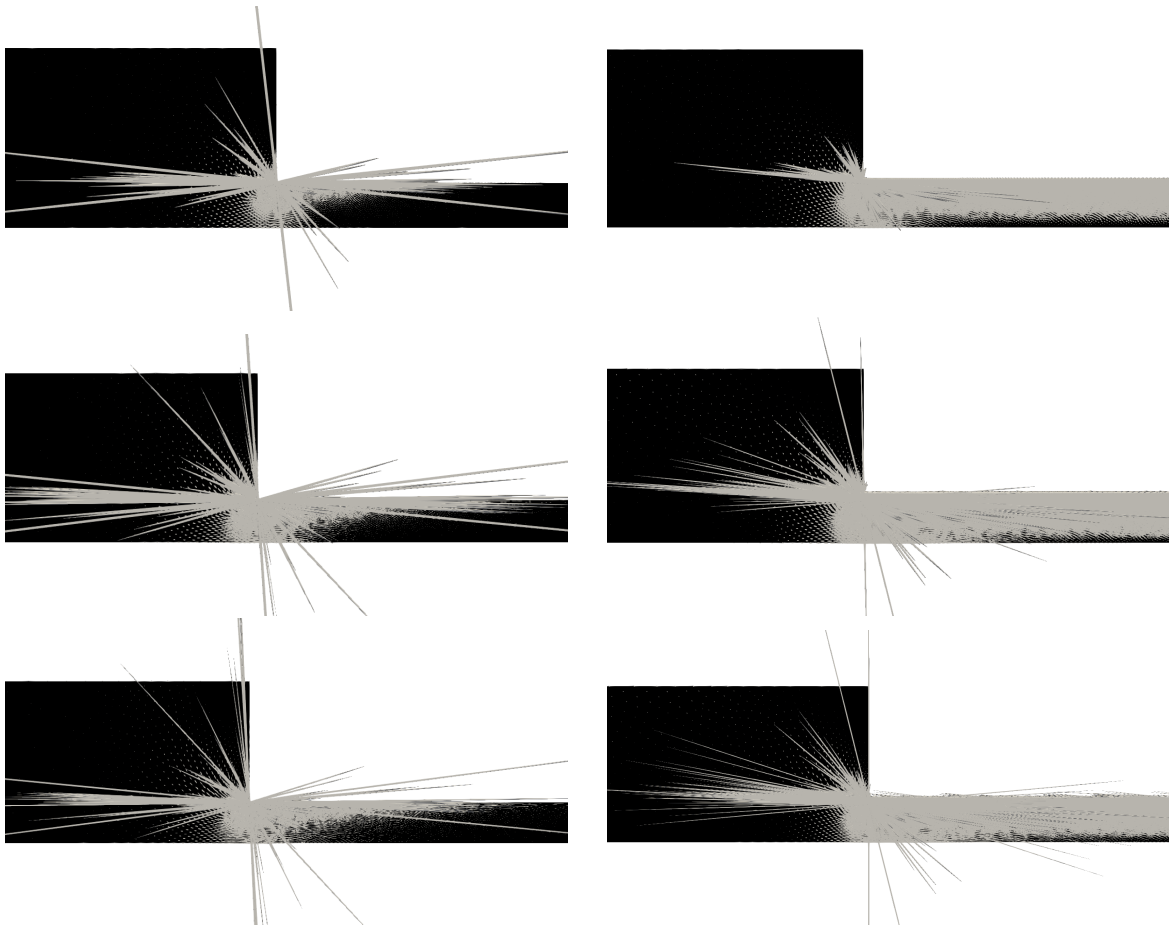

Figure 3.16: Deformation tensor in slip (left) and stick (right) case. From above to below: $We = 1, 2, 3$.

Chapter 4

Comparison with biological data

4.1 Abstract

In this last chapter, we focus on the data of the paper *A microfluidic platform to investigate the role of mechanical constraints on tissue reorganization* [1] by Sham Tlili, François Graner and Hélène Delanoë-Ayari. Luckily, I had the possibility to meet them and discuss interesting ideas and results. Moreover, these authors transmitted me the numerical data associated to experiments. The objective of this chapter is to compare these experimental data with the numerical results obtained with the Oldroyd-B model and to identify the most suitable Weissenberg number associated to this model. This is accomplished by comparing the velocity fields and analyzing cell elongation using the conformation tensor.
Their experiments are characterised by slip at the wall, so in this chapter the slip boundary conditions are taken into account. To be more precise, in the paper they utilise an aggregate called embryonic carcinoma F9 to study 3D tissues cell group scale mechanical properties. The experimental setup involves placing the aggregate into a cone-shaped pipette, which then allows it to settle in a reservoir with a height of 100 μm. After a minimum waiting period of 10 minutes for stress relaxation, the aggregate is pushed towards the entrance of the channel. Due to the applied pressure difference, it undergoes deformation at the entrance of the small channel, allowing the researchers to observe and analyze its mechanical behaviour (see Figure 4.1).

4.2 Estimation of the Weissenberg number using the relaxation length

The velocity data were subject to some preprocessing steps. Specifically, the data was organized in a square grid format, where for each pair of coordinates (x, y) we had the velocity components

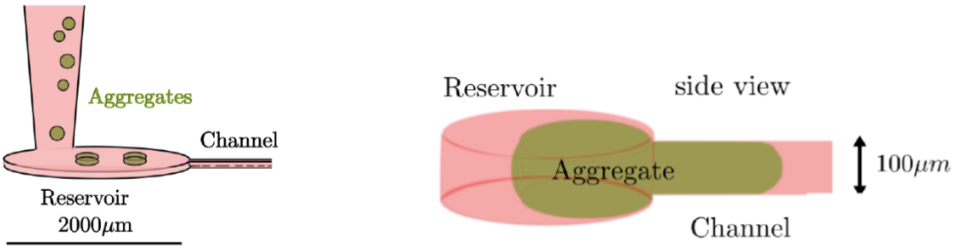

Figure 4.1: Experiments setting: the aggregate passes into the cone pipette and lies in the reservoir, then it is aspirated through the small channel. Figure from the paper [1]

(u_x, u_y). To facilitate comparison with the numerical results obtained in previous chapters, the data was made dimensionless. Given the known width of the small channel (100 μm) , the y coordinate was rescaled by dividing it by half the channel width, i.e., 50 μm. Indeed, it's worth recalling that, for the abrupt contraction geometry, the width of half the small channel was normalized to 1. The same process was applied to the x coordinate since the grid was equispaced in both directions. Lastly, the origin was recentered according to the abrupt contraction geometry.
Regarding the rescaling of the velocity field, the objective was to ensure that the values of velocity at the most downstream points averaged vertically to one. However, due to the challenges in measurement, the available data for the small channel was limited to near the entrance. Therefore, imposing the values on the left side to average one vertically may not be perfectly precise but this approach still yielded interesting results.
Figure 4.2 compares in paraview the vector norm of the velocity field obtained with experimental data and with the numerical implementation, choosing $We = 2$. We can notice that the magnitudes are similar, with a peak of the velocity at the entrance of the channel. In addition. we can visualise the streamlines of both the vector fields and notice that, while in the numerical results the vortices appears in the corners, in the experimental data this phenomenon does not occur (see Figure 4.3). This is probably due to the fact that the aggregate does not reach the corners of the domain, since the reservoir has a circular section.
Figure 4.4 considers the velocity components profile along the axis of symmetry: it seems that the experimental data align with the numerical results, although with a slightly lower peak value at the entrance. This difference could be attributed to the averaging of measurements taken from small cell groups.
The same procedure can be used along the vertical direction as well: Figure 4.5 compares the two components of the velocity field with the experimental data. To sum up, it is important to note that the overall trend of the curves appears to be consistent, but it is difficult to determine the most appropriate Weissenberg number just by looking at these figures. However, particularly in the vertical direction, some points are clearly aligned with a Weissenberg number of 2.

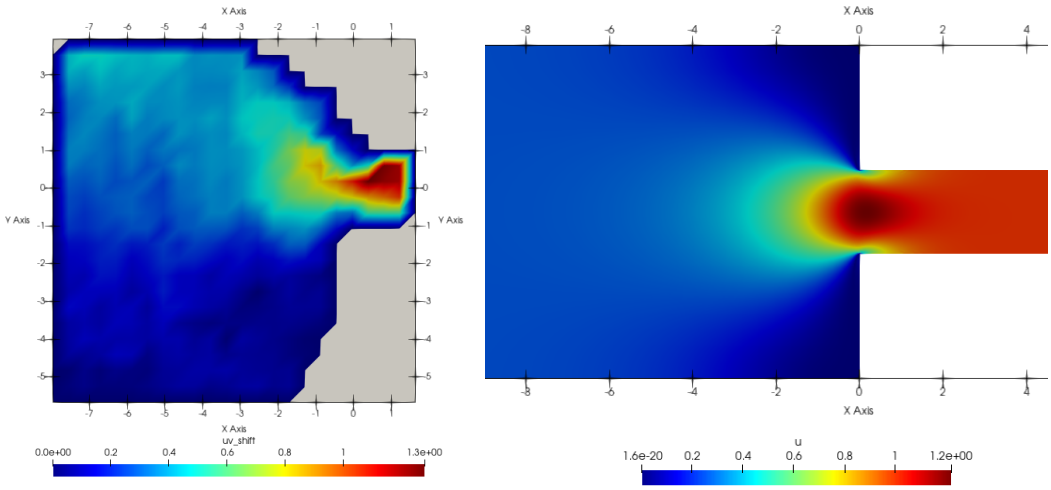

Figure 4.2: Representation of the magnitude of the velocity field using the experimental data of paper [1] (right) and the numerical simulation (left) with $We = 2$. For the experimental data, the area in grey corresponds to the NaN values, which are cells in the grid outside the aggregate.

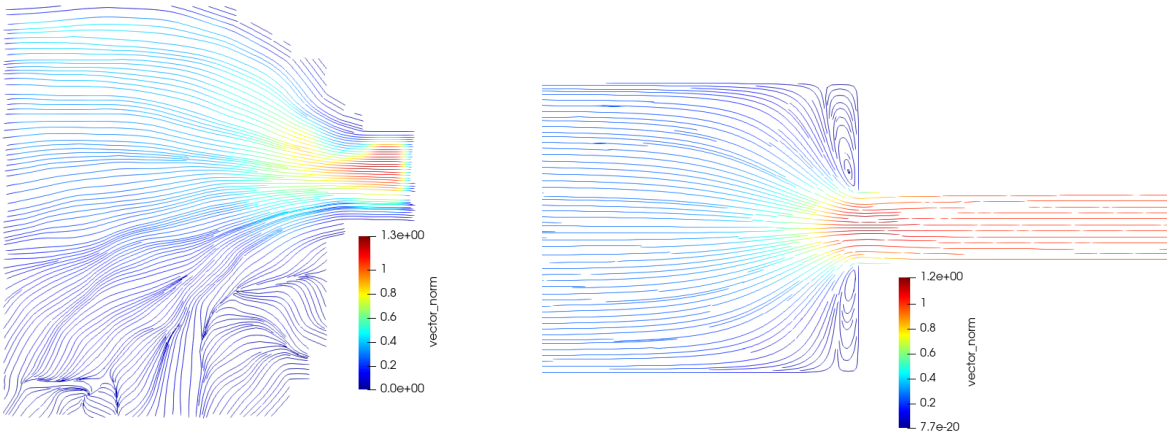

Figure 4.3: Representation of the streamlines of the velocity field using the experimental data of paper [1] (right) and the numerical simulation (left) with $We = 2$.

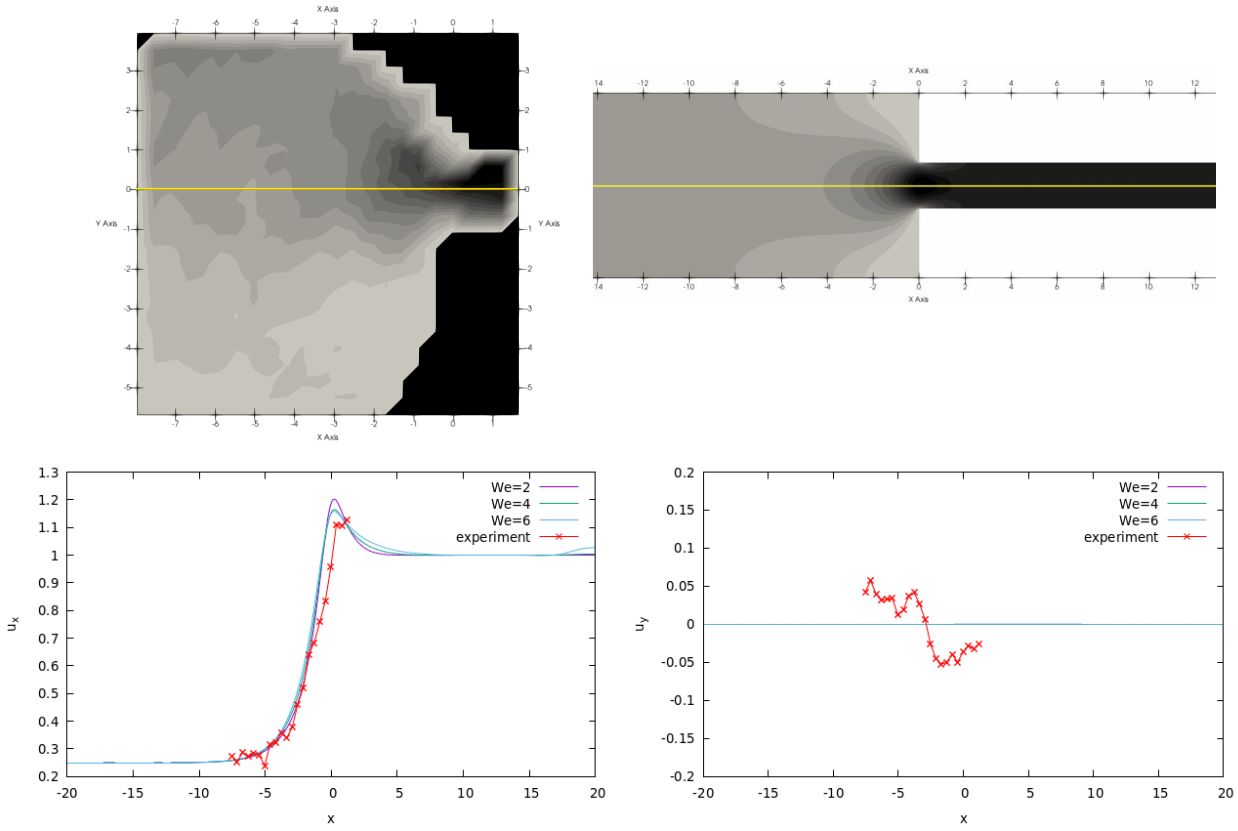

Figure 4.4: Velocity cut in the horizontal axis of symmetry. Top left and right: representation if the axis along which the cut is applied. Bottom left: x component, bottom right: y component.

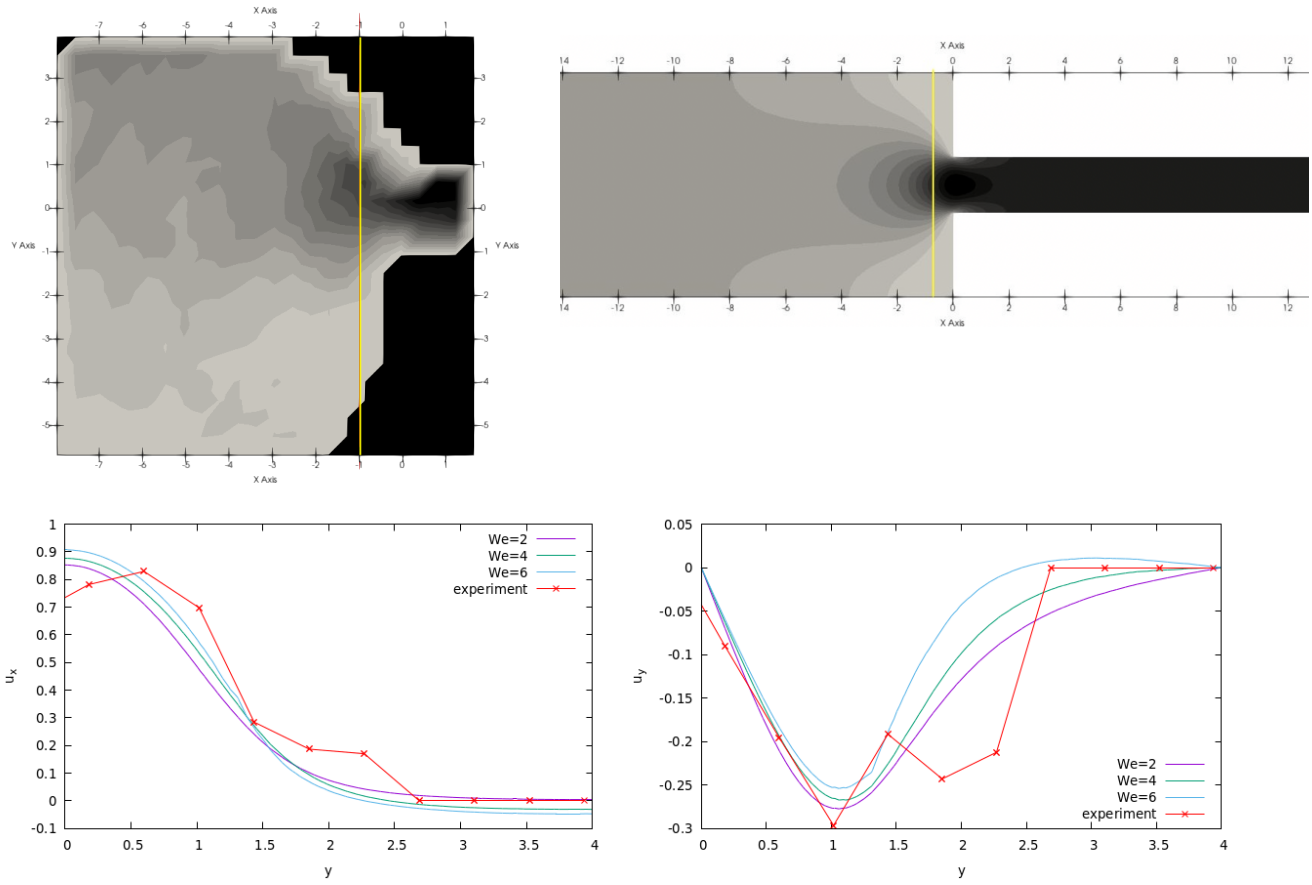

Figure 4.5: Velocity cut in the vertical axis next to the corner. Top left and right: representation if the axis along which the cut is applied. Bottom left: x component, bottom right: y component.

A more effective approach for selecting the most appropriate Weissenberg number involves analyzing the deformation tensor. However, due to limitations in measurements, it has not been possible to deeply investigate the small channel, causing a challenge when comparing results because the peak deformation in the small channel is not clearly defined. However, some interesting plots have been generated.

Firstly, we can compare the deformations by plotting the experimental and numerical deformation tensors, as shown in Figures 4.6-4.10. It is important to note that a threshold on the maximum deformation value has been applied to avoid the explosion of the numerical tensor in the corner cells. While it could be difficult to draw definitive conclusions, an important result is that for $We = 1$, the cells relax almost immediately at the entrance, while in the experimental data, there is a deformation of 1.5 units at $x = 0.5$. This suggests that a Weissenberg number greater than 1 may be more appropriate. Taking into account $We = 2$, between $x = 0.5$ and $x = 1$ the magnitude of the deformation tensor is around 2, and, for the data, at the same position we have a value between 1.5 and 2. Based on this observation, a Weissenberg number closed to 2 can suit well.

To go further into the details, we can cut the deformation tensors in various directions and compare them. The first direction is along the horizontal axis of symmetry. As previously mentioned, these plots have limitations due to incomplete data, making it difficult to observe the maximal value reached by the deformation at downstream. The results are presented in Figure 4.11.

Nevertheless, we are able to conclude that the maximal value of the deformation is higher than that at $We = 1$, indicating that $We > 1$ should be considered. Additionally, it is worth noting that the shear deformation is not consistently zero along the axis of symmetry in the experimental data, which could be attributed to the loss of symmetry of the observed experimental flow.

The second direction focuses on the vicinity of the entrance, as depicted in Figure 4.12. Here, especially in the sum and difference plots, we can observe that the peaks of the experimental data have a magnitude similar to the numerical results at $We = 2$, while for the shear component, the experimental data align more closely with $We = 1$.

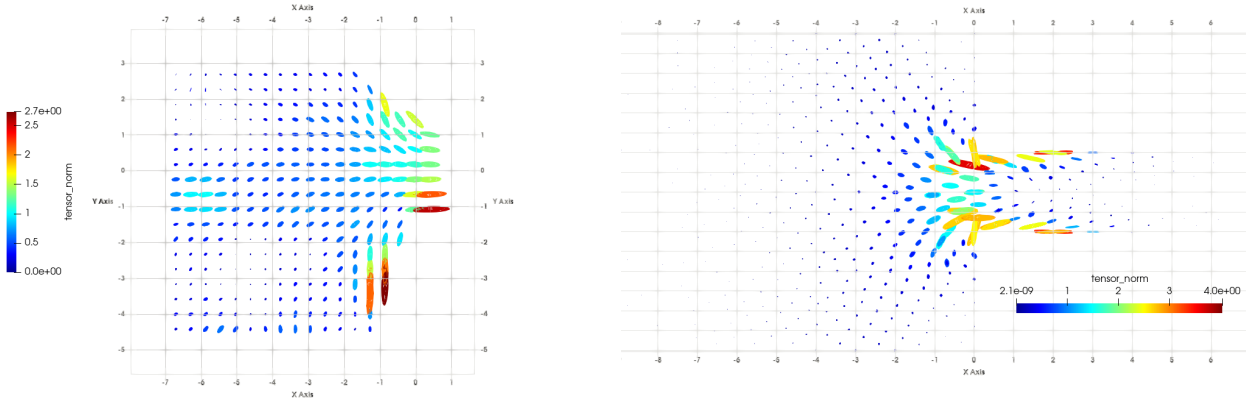

Figure 4.6: Representation of the deformation tensor. Left: data, right: numerics with $We = 1$.

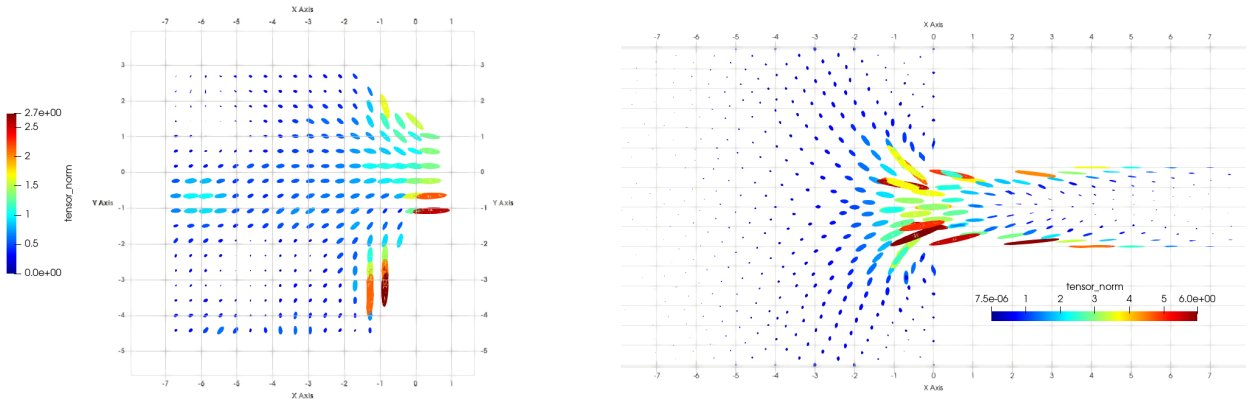

Figure 4.7: Representation of the deformation tensor. Left: data, right: numerics with $We = 2$.

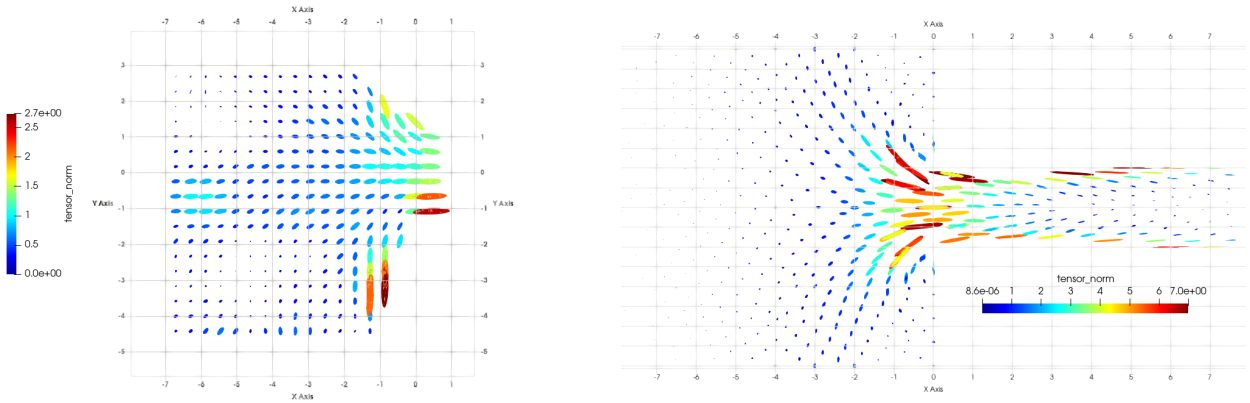

Figure 4.8: Representation of the deformation tensor. Left: data, right: numerics with $We = 3$.

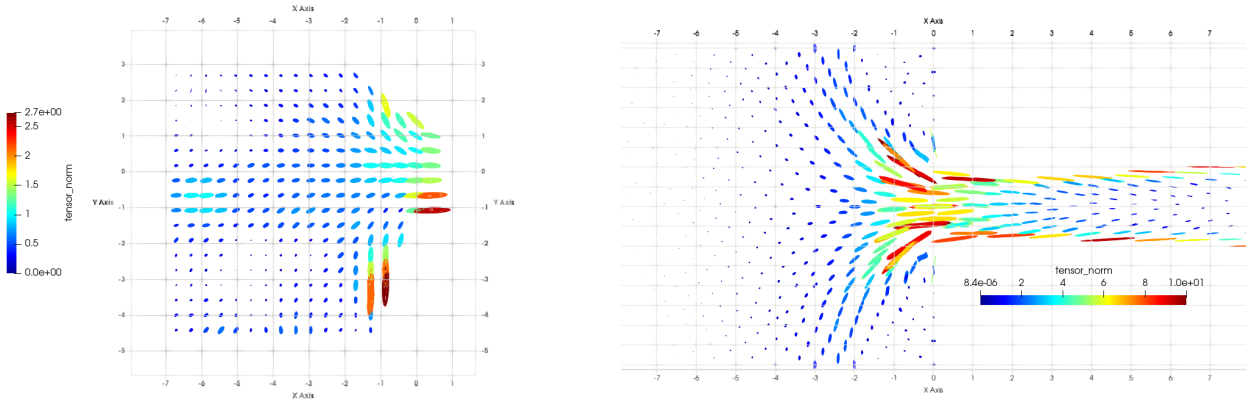

Figure 4.9: Representation of the deformation tensor. Left: data, right: numerics with $We = 4$.

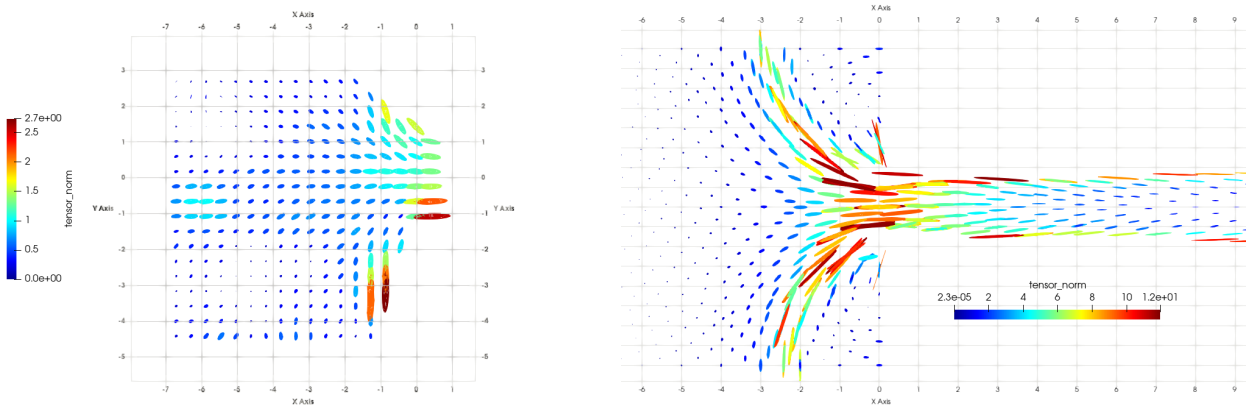

Figure 4.10: Representation of the deformation tensor. Left: data, right: numerics with $We = 6$.

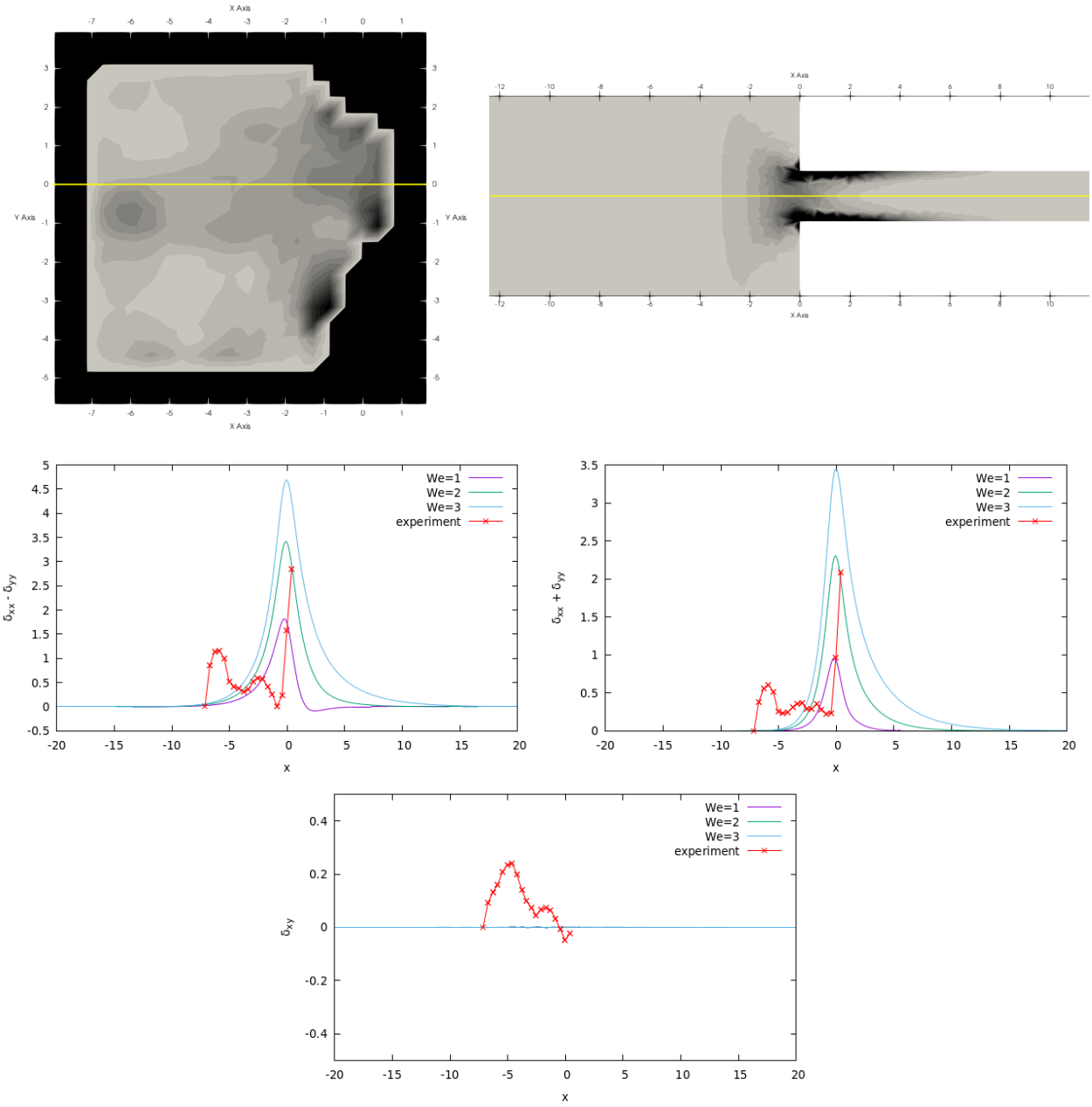

Figure 4.11: Cut of the deformation tensor along the horizontal axis.

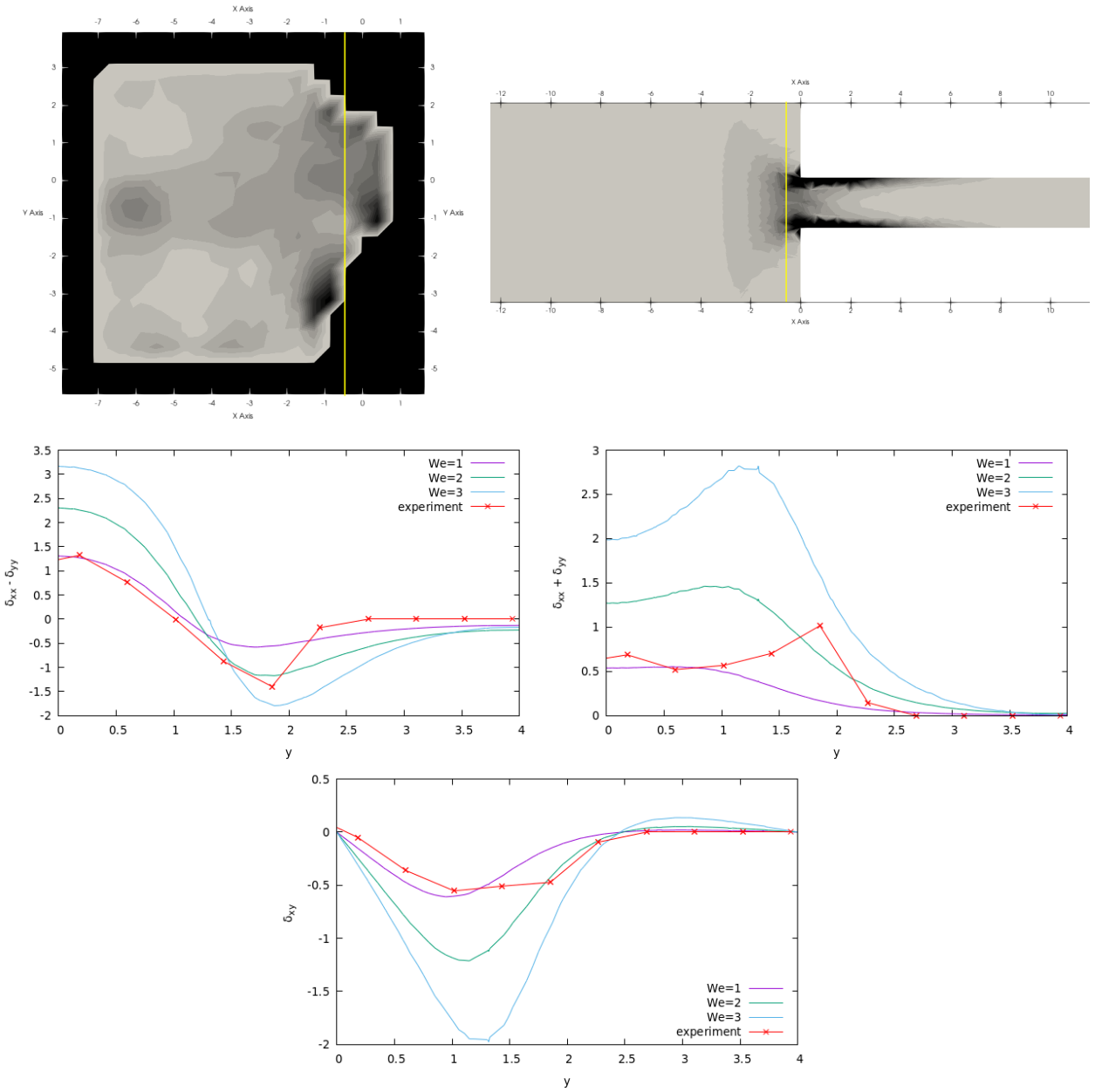

Figure 4.12: Cut of the deformation tensor along the vertical axis.

Chapter 5

Conclusion

To sum up, the application of the Oldroyd-B model captures interesting aspects of the observed behaviour in the data. Especially comparing the velocity fields, we can find many similarities in the magnitude and trends of the plots obtained by analyzing the field in important directions. However, to draw meaningful conclusions about the deformation tensor, we need more data. From observing the behaviour at the entrance, we can conclude that a Weissenberg number greater than 1 is necessary. Determining the upper limit is challenging without data on the relaxation length and peak deformation but, by only considering the magnitude of cell elongation at the entrance, it seems reasonable to choose a Weissenberg number less than 3. In conclusion, the most suitable Weissenberg number appears to be around 2.

It is important to acknowledge a limitation of the model, which is the explosion of the deformation tensor at the corner singularity, not aligned with the bounded stretch observed in the experimental data. To address this limitation, alternative approaches can be considered. One possible solution involves utilizing the FENE-P model, which bounds the deformation tensor. Another way for improvement involves introducing plasticity into the fluid equations. By incorporating plastic behaviour, the material's response can be controlled and limited, allowing for a more accurate representation of the experimental data. This could be a starting point for future works.

Appendix A

Slip boundary conditions

Recall the geometry of the problem in Figure A.1.

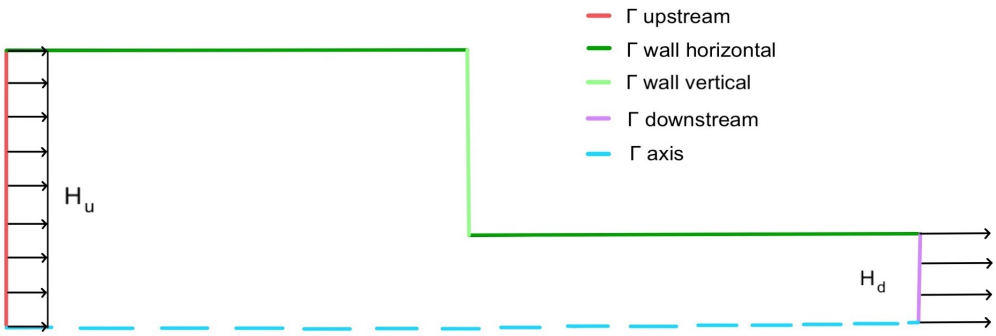

Figure A.1: Geometry of the problem

Let now study the slip boundary conditions.
First, we impose the upstream and downstream velocities $\mathbf{u}_\mathrm{u}$ and $\mathbf{u}_\mathrm{d}$. Due to the slip condition, the velocity is constant in the x-direction and zero in the y-direction. Specifically, the flow rate should be conserved, and thus, we require that $\mathrm{H_u} \cdot \mathbf{u}_\mathrm{u} = \mathrm{H_d} \cdot \mathbf{u}_\mathrm{d}$, where $\mathrm{H_u}$ and $\mathrm{H_d}$ are the height of sections at the upstream and downstream, respectively. To simplify the problem, we normalize the downstream velocity by setting $\mathbf{u}_\mathrm{d} = [1, 0]^T$, which leads to $\mathbf{u}_\mathrm{u} = [\mathrm{H_d}/\mathrm{H_u}, 0]^T$.
The slip boundary conditions read:

$$\begin{aligned} \mathbf{u}.\mathbf{n} = 0 \text{ and } \boldsymbol{\tau}_{nt} = 0 \text{ in } \Gamma_{\text{wall-vertical}} \cup \Gamma_{\text{wall-horizontal}} \cup \Gamma_{\text{axis}}, \\ \mathbf{u}_t = 0 \text{ and } \boldsymbol{\tau}_{nn} = 0 \text{ in } \Gamma_{\text{upstream}}, \\ \mathbf{u} = [1, 0] \text{ in } \Gamma_{\text{downstream}}. \end{aligned} \tag{A.1}$$

Let now compute $\mathbf{u}.\mathbf{n}$, $\boldsymbol{\tau}_{nt}$ and $\boldsymbol{\tau}_{nn}$. Recall that we can always split a vector into normal and

tangential components:

$$\mathbf{u} = \mathbf{u}_n + \mathbf{u}_t = (\mathrm{u} \cdot \mathrm{n})\mathbf{n} + \mathbf{u}_t,$$

$$\boldsymbol{\tau} \cdot \mathbf{n} = \boldsymbol{\tau}_{nn} + \boldsymbol{\tau}_{nt} = ((\boldsymbol{\tau} \cdot \mathrm{n}) \cdot \mathrm{n})\mathbf{n} + \boldsymbol{\tau}_{nt}$$

Consider now the vertical wall, where $\mathbf{u} = u_x \mathbf{e_x} + \mathbf{u}_t$. Then

$$\boldsymbol{\tau} \cdot \mathbf{n} = \begin{bmatrix} \boldsymbol{\tau}_{xx} & \boldsymbol{\tau}_{xy} \\ \boldsymbol{\tau}_{xy} & \boldsymbol{\tau}_{yy} \end{bmatrix} \cdot \begin{bmatrix} 1 \\ 0 \end{bmatrix} = \begin{bmatrix} \boldsymbol{\tau}_{xx} \\ \boldsymbol{\tau}_{xy} \end{bmatrix} = \begin{bmatrix} \boldsymbol{\tau}_{xx} \\ 0 \end{bmatrix} + \begin{bmatrix} 0 \\ \boldsymbol{\tau}_{xy} \end{bmatrix} = ((\boldsymbol{\tau} \cdot \mathrm{n}) \cdot \mathrm{n})\mathbf{n} + \boldsymbol{\tau}_{nt}$$

Thus, using (A.1), we can impose the boundary conditions in the vertical wall:

$$u_x = 0 \text{ and } \boldsymbol{\tau}_{xy} = 0 \text{ in } \Gamma_{\text{wall-vertical}} \tag{A.2}$$

The same procedure can be done for the horizontal and the axis wall, obtaining:

$$u_y = 0 \text{ and } \boldsymbol{\tau}_{xy} = 0 \text{ in } \Gamma_{\text{wall-vertical}} \cup \Gamma_{\text{axis}} \tag{A.3}$$

Finally, condering equation (2.7), we can impose the boundary conditions on $\boldsymbol{\chi}$. If $\boldsymbol{\tau} = 0$, we obtain

$$\boldsymbol{\chi} = \frac{\eta_p}{a\lambda} \log\left(\mathbf{I} + \frac{a\lambda}{\eta_p} \cdot 0\right) = \frac{\eta_p}{a\lambda} \log\left(\mathbf{I}\right) = 0$$

Bibliography

[1] S. L. Tlili, F. Graner, and H. Delanoë-Ayari, "A microfluidic platform to investigate the role of mechanical constraints on tissue reorganization," *Development*, vol. 149, no. 20, p. dev200774, 2022.

[2] J. Oldroyd, "On the formulation of rheological equations of state," *Proceedings of the Royal Society of London. Series A. Mathematical and Physical Sciences*, vol. 200, no. 1063, pp. 523–541, 1950.

[3] R. Fattal and R. Kupferman, "Constitutive laws for the matrix-logarithm of the conformation tensor," *J. Non-Newt. Fluid Mech.*, vol. 123, no. 2, pp. 281–285, 2004.

[4] ——, "Time-dependent simulation of viscoelastic flows at high weissenberg number using the log-conformation representation," *J. Non-Newt. Fluid Mech.*, vol. 126, no. 1, pp. 23–37, 2005.

[5] P. Saramito, "On a modified non-singular log-conformation formulation for johnson–segalman viscoelastic fluids," *J. Non-Newt. Fluid Mech.*, vol. 211, pp. 16–30, 2014.

[6] ——, *Efficient C++ finite element computing with Rheolef*. CNRS-CCSD ed., 2020, http://hal.archives-ouvertes.fr/cel-00573970.

[7] M. A. Hulsen, "A sufficient condition for a positive definite configuration tensor in differential models," *J. Non-Newt. Fluid Mech.*, vol. 38, no. 1, pp. 93–100, 1990.

[8] T. E. Jamal, "Numerical resolution of viscoelastic fluids. simulation of a flow in abrupt contraction," 2020.

[9] P. Saramito, *Complex fluids*. Springer, 2016.

[10] R. Comminal, J. Hattel, M. Alves, and J. Spangenberg, "Vortex behavior of the oldroyd-b fluid in the 4-1 planar contraction simulated with the streamfunction–log-conformation formulation," *J. Non-Newt. Fluid Mech.*, vol. 237, pp. 1–15, 2016.